The liquid-vapour interface of pure fluids and mixtures: application of computer simulation and density functional theory

The liquid–vapour interface of pure fluids and mixtures: application of computer simulation and density functional theory

J Winkelmann

Institut für Physikalische Chemie, Martin-Luther Universität Halle-Wittenberg,
D-06217 Merseburg, Germany

Abstract

In this work we present and discuss new molecular dynamics simulation procedures and the application of density functional theory to the liquid–vapour interface of pure fluids and their liquid mixtures. Our aim was to further investigate the simulation set-up and parameters to obtain reliable simulation data for the phase behaviour, interfacial structure and surface tension. The influence of box geometries and summation techniques is discussed.

In the application of the density functional theory we analysed the influence of different approximations within the theory on the calculation of interfacial behaviour and optical properties. In particular, the attractive free-energy term of a local density functional approach is modified by introducing an analytical representation of the radial distribution function of the uniform reference fluid. The calculated liquid and gas densities and surface tensions are in good agreement with recent molecular dynamics simulations. But the results clearly show that capillary-wave contributions, acting on different scales of length and time, have to be taken into consideration in predicting both surface tensions and optical properties such as ellipticity and specular reflectivity.

(Some figures in this article are in colour only in the electronic version; see `www.iop.org`)

1. Introduction

Due to their fundamental importance in nature, liquid–vapour and liquid–liquid interfaces have attracted the attention of scientists over the last few decades. Apart from its theoretical interest, a detailed understanding of interfacial behaviour in liquids is crucial to many technological processes, such as coating or adsorption, industrial separation and tertiary oil recovery. In recent years there has been rapidly growing interest in surface properties of micellar and membrane systems [1]. Considerable effort has been made but an adequate description and modelling of surfaces and interfacial properties of more complex systems within their experimental accuracy is still far from being achieved. There is some progress towards bridging the gap between statistical mechanics of inhomogeneous fluid systems, thermodynamic and phase behaviour and experimental optical methods in surface chemistry. In addition to

theoretical methods [1–18], computer simulations [19–24] have become more and more important as a tool for obtaining information on bulk properties of fluids and mixtures as well as on their interfacial structure and behaviour. There is a comprehensive and critical review on simulations of the liquid–vapour interface in Lennard-Jones fluids, where Trokhymchuk and Alejandre [25] studied the influence of system size and truncation of interaction potential on different simulation techniques and their results. For mixtures, direct surface simulations can predict the phase equilibria. Thus the Gibbs-ensemble Monte Carlo method [26] and the NpT + test-particle method [27] provide a good opportunity to test the performance of the surface simulation. Besides performing a direct determination of phase equilibria, we obtain information on the internal structure of these fluid interfaces. Theoretical predictions give partial density profiles which in certain concentration ranges show enrichment of one component in the interface. These concentration profiles might act as driving forces for a molecular diffusive transport process and thus determine the phase transition kinetics. Unfortunately, there is no direct experimental proof of these results. Therefore, we consider our direct surface simulations as an appropriate tool for producing pseudo-experimental data which, within the same intermolecular interaction potential model, can verify these internal structures and concentration profiles.

Serious problems occur when turning to dipolar fluids due to their long-ranged electrostatic interactions. Conventional three-dimensional Ewald summation requires a periodic laminar simulation box (see figure 1(c)) [28–30], whereas an interfacial system with periodic boundary conditions in only two dimensions (figure 1(b)) leads to expressions in lattice summation which are much harder to implement efficiently into the simulation code [31, 32].

One of the most popular approaches to statistical mechanics of inhomogeneous fluids is the density functional theory (DFT) [1–10] as an alternative to integral equation theories [11–18]. In the simple local density approximation (LDA) to density functional theory, which is used in many applications, short-range correlations of molecules in the interface are neglected. This is known to be a rather poor approximation for fluids near walls or adsorption in porous systems [2, 4–6, 33]. But for free liquid interfaces the LDA seems to be a reasonable approach in modelling interfacial behaviour. To include local structuring and short-ranged correlations around a given particle, a number of different approximate functionals within the smoothed-density approximation (SDA) [2, 4, 5, 8, 34] were developed which provide a more realistic treatment of fluid interfaces and which may affect interfacial properties predicted.

Unlike the situation for the repulsive part, little had been done to improve the description of the attractive contributions to the free energy over the traditionally used mean-field (MF) approximation. In this MF *ansatz* the pair correlation function of the particles is assumed to be unity, which leads to a poor description of the influence of the attractive forces upon the bulk fluid properties and results in a rather wrong phase equilibrium [40]. The calculated liquid densities are always too low. Thus the computed surface tensions and interfacial properties cannot directly be compared with molecular dynamics simulation results or with experimental data and fitting of potential parameters to surface tension data is no remedy for the deficiencies of the theory.

Since there is no direct experimental method to prove the interfacial structures calculated from either LDA or SDA models we look for suitable experiments whose results can be predicted by DFT calculations. Optical techniques like specular x-ray reflectivity or ellipsometry are important for probing surface structures on length scales down to a few nanometres. Thus, specular reflectivity has been used to determine the structural behaviour of molecules adsorbed at interfaces as well as interfacial roughness due to thermally excited capillary waves [35–37]. We compare these experiments with our predictions and hope to find additional evidence for the quality of our theoretical models.
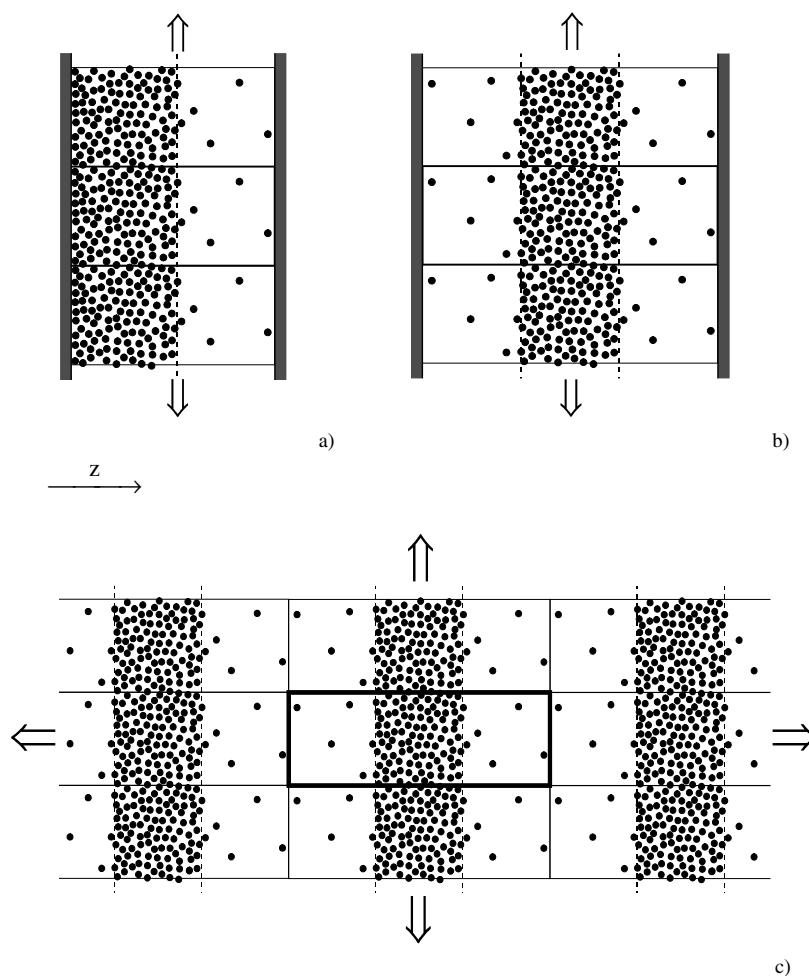
Figure 1. Different geometries for a simulation box set-up in a vapour–liquid interfacial system: (a) a system with hard walls in the z-direction and periodic boundaries in the x–y plane; (b) a vapour–liquid–vapour arrangement with two-dimensional periodic conditions; (c) a laminar vapour–liquid–vapour system with three-dimensional periodicity.

2. Molecular dynamics simulations

2.1. Simulation techniques for Lennard-Jones systems

From some of the earlier simulation studies we find a considerable variation of results, especially for the surface tension, caused by problems in the simulation set-up or by insufficient simulation time. The correct choice of simulation conditions is of fundamental importance for obtaining accurate and consistent results. We performed simulations on a three-dimensional liquid in equilibrium with its vapour. The molecules interact via a Lennard-Jones potential:

$$u_{ij}^{LJ}(r_{12}) = 4\varepsilon_{ij}\left[\left(\frac{\sigma_{ij}}{r_{12}}\right)^{12} - \left(\frac{\sigma_{ij}}{r_{12}}\right)^{6}\right]. \tag{1}$$

To describe interactions between different species of molecules in mixtures when $i \neq j$ we apply the mixing rules

$$\varepsilon_{ij} = (1 - k_{ij})\sqrt{\varepsilon_{ii}\varepsilon_{jj}}$$

$$\sigma_{ij} = (1 - l_{ij})(\sigma_{ii} + \sigma_{jj})/2 \tag{2}$$

and introduce empirical binary parameters k_{ij} and l_{ij} to account for deviations from these mixing rules. The parameters used are given in table 1.

Table 1. Lennard-Jones potential parameters ε/k and σ used in molecular dynamics simulations of binary mixtures [39].

	Pure fluids		
Substance	ε/k (K)	σ (Å)	
Argon	117.05	3.3967	
Methane	148.99	3.7275	
	Mixture		
	ε_{12}/k (K)	k_{12}	σ_{12} (Å)	l_{12}
Argon–methane	127.304	0.03600	3.5671	−0.00141

We use the following definitions of reduced quantities [38]: reduced temperature $T^* = kT/\varepsilon$, reduced length $z^* = z/\sigma$, reduced density $\rho^* = \rho\sigma^3$ and reduced surface tension $\gamma^* = \gamma\sigma^2/\varepsilon$. In the case of a binary mixture the reduced quantities will be scaled with respect to the potential parameters of component 1 [39]. Our simulations were performed in an NVT ensemble, i.e., at prescribed particle number, volume and temperature with different cut-off radii r_c. The temperature was kept constant by the momentum scaling method and the equations of motion were solved using a fifth-order predictor–corrector algorithm. The reduced time step Δt^* was varied from 0.002 to 0.005 in units of $\sigma\sqrt{m/\varepsilon}$.

The simulation procedure was started from a fcc lattice in a cubic box. We chose a density slightly higher than the appropriate liquid density, which was available from our equation of state [41]. This choice causes the liquid film to have approximately the thickness of the cubic start box. After a short melting and equilibration period the simulation system was completed by two empty cells on both sides in the z-direction so that a laminar box arrangement as in figure 1(c) resulted. In the case of a mixture the cell dimensions were $z = 3x = 3y$ with particle numbers between 2048 and 2916 to employ the desired cut-off radii. After the interfacial system was equilibrated over 400 000 time steps the production period of 300 000 steps was instigated during which the coexisting densities and the surface tension were evaluated. The block average method [42] was used to perform the statistical uncertainties of the computed surface tension values. Since some mixtures still showed slightly asymmetric partial density profiles at the end of this period, some of the production runs were extended by another 300 000 time steps.

We applied periodic boundary conditions in the x–y plane. In the z-direction one can use either periodic boundary conditions (figure 1(c)) or hard reflecting walls (figures 1(a), 1(b)). Although using the hard-wall system seems to be a realistic approach, such a system is more difficult to handle. Collisions of vapour-phase particles with the hard wall induce an additional momentum which especially at higher temperatures can cause the centre of mass to move strongly. These movements have to be corrected for by allowing the reference frame to move attending to particles close to the walls. When running the simulation with complete

periodic boundary conditions (figure 1(c)) we only observe a negligible displacement of the centre of mass which can easily be corrected. Furthermore, the collision of a particle with the wall in the presence of another force within its cut-off radius is not exactly calculable by means of a predictor–corrector algorithm. However, we have performed simulations with both models and we found no significant differences either in the density profiles or in the surface tension results. In order to correct for the influence of the cut-off radius, Lotfi *et al* [43] suggested long-range corrections (LRC) to the dynamics. We found [38, 39] that they work well with small r_c but do not influence the density profile if $r_c \geqslant 6\sigma$.

2.2. Surface tension and tail correction procedures

During simulation the surface tension was calculated using the virial expression [22, 39, 44]

$$\gamma = \frac{1}{2A} \left\langle \sum_{\substack{i < j \\ r < r_c}} \left(r_{ij} - \frac{3z_{ij}^2}{r_{ij}} \right) u'(r_{ij}) \right\rangle \tag{3}$$

where A is the total surface area ($A = 2xy$), $u'(r_{ij})$ is the derivative of the pair potential and the angle brackets denote a time average. The summation extends over all particles within the cut-off radius r_c. Even though we are using a rather large $r_c = 7.0\sigma$, there is still a considerable tail contribution to the surface tension to be expected which arises from the contribution of the potential for distances larger than r_c. A widely used *ansatz* for calculating this tail contribution γ_{tail} was given by Chapela *et al* [21], and later corrected by Blokhuis *et al* [45]. But its application to mixtures causes some problems. Therefore we proposed a new algorithm [38] for computing γ_{tail} directly within the simulation. We calculate an individual tail contribution γ_i^{tail} for each particle i at each time step within the simulation run, and form the average

$$\gamma_{\text{tail}} = \frac{1}{2A} \left\langle \sum_{\substack{i \\ r > r_c}} \gamma_i^{\text{tail}} \right\rangle.$$

In order to determine γ_i^{tail} we apply the virial route formula given by equation (3) to the interactions of a particle i in the simulation box with all particles outside its cut-off sphere in an infinite volume. These particles are now replaced by the current-density profile. In the case of a binary mixture the partial density profiles are used. For each particle i the tail contributions arising from both components A and B are calculated separately and added together. This enables us to take into account the different interaction parameters. Using spherical coordinates and considering the homogeneity of the system in the xy-direction we obtain for γ_i^{tail} for a component-A particle

$$\gamma_{i(\text{A})}^{\text{tail}} = -24\pi \int_{r=r_c}^{\infty} \mathrm{d}r \left(2\left(\frac{1}{r}\right)^{12} - \left(\frac{1}{r}\right)^6 \right)$$

$$\times r^2 \int_0^{\pi} \mathrm{d}\vartheta \ (1 - 3\cos^2\vartheta) \sin\vartheta \ \rho_{\text{A}}(z_i + r\cos\vartheta)$$

$$- 24\pi \int_{r=r_c}^{\infty} \mathrm{d}r \ \frac{\varepsilon_{\text{AB}}}{\varepsilon_{\text{A}}} \frac{\sigma_{\text{A}}}{\sigma_{\text{AB}}} \left(2\left(\frac{\sigma_{\text{AB}}/\sigma_{\text{A}}}{r}\right)^{12} - \left(\frac{\sigma_{\text{AB}}/\sigma_{\text{A}}}{r}\right)^6 \right)$$

$$\times r^2 \int_0^{\pi} \mathrm{d}\vartheta \ (1 - 3\cos^2\vartheta) \sin\vartheta \ \rho_{\text{B}}(z_i + r\cos\vartheta)$$

and for γ_i^{tail} for a component-B particle

$$\gamma_{i(B)}^{\text{tail}} = -24\pi \int_{r=r_c}^{\infty} dr \; \frac{\varepsilon_{AB}}{\varepsilon_A} \frac{\sigma_A}{\sigma_{AB}} \left(2\left(\frac{\sigma_{AB}/\sigma_A}{r} \right)^{12} - \left(\frac{\sigma_{AB}/\sigma_A}{r} \right)^6 \right)$$
$$\times \; r^2 \int_0^{\pi} d\vartheta \; (1 - 3\cos^2\vartheta) \sin\vartheta \; \rho_A(z_i + r\cos\vartheta)$$
$$- 24\pi \int_{r=r_c}^{\infty} dr \; \frac{\varepsilon_B}{\varepsilon_A} \frac{\sigma_A}{\sigma_B} \left(2\left(\frac{\sigma_B/\sigma_A}{r} \right)^{12} - \left(\frac{\sigma_B/\sigma_A}{r} \right)^6 \right)$$
$$\times \; r^2 \int_0^{\pi} d\vartheta \; (1 - 3\cos^2\vartheta) \sin\vartheta \; \rho_B(z_i + r\cos\vartheta).$$

In both equations the first terms come from the interactions of particle i with component-A particles and the last terms from those with component-B particles. The parameters for the numerical integration and the integration method correspond to those used in the simulation of pure fluids [31, 38]. Results for the reduced surface tension of a Lennard-Jones fluid with tail corrections are shown in figure 2. We clearly see that the values converge for $r_c \geqslant 5\sigma$ at the 'exact' value of γ^* for the microscopic system. A comparison with experimental data for krypton, however, reveals that there is still a larger difference between simulation and experiment. This indicates that contributions from different length scales, i.e. capillary-wave contributions, may be needed to correct for these discrepancies.
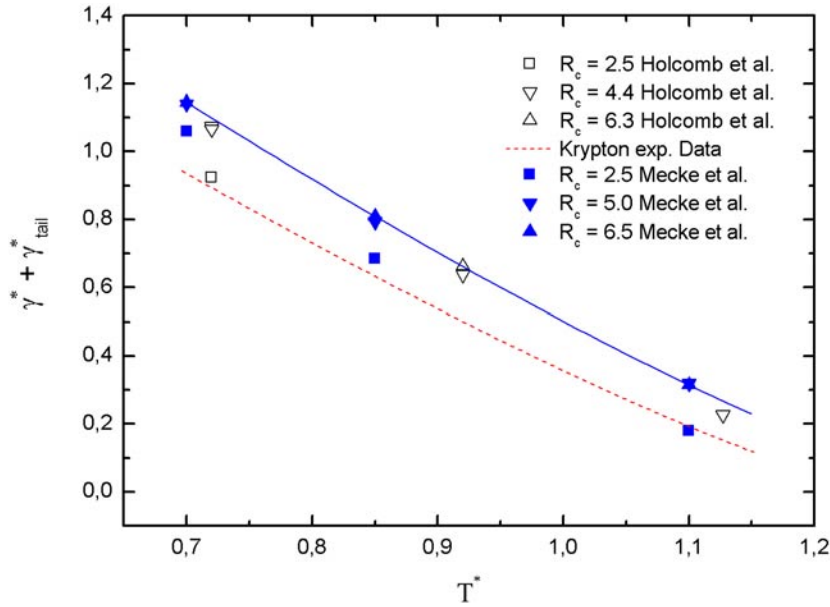

Figure 2. Reduced surface tension for a Lennard-Jones fluid with tail correction $\gamma^* + \gamma_{\text{tail}}^*$ versus reduced temperature obtained from our simulations in comparison with simulation data of Holcomb *et al* [24]. The solid line relates to the limit of convergence. The dashed line shows experimental results for krypton.

2.3. Non-spherical and dipolar molecule systems

The application of our simulation strategy to non-spherical two-centre Lennard-Jones fluids is a straightforward extension. The size of the simulation box has to be selected so that the larger

molecules may move freely within the liquid phase. We therefore used $z = 6x = 6y$ and 2744 particles with a cut-off radius $r_c = 6.3\sigma$. Tail corrections to the surface tension were made in the way described above. The simulated phase equilibria agree very well with our previous results on homogeneous fluids using the NpT + test-particle method [46]. To generalize the resulting surface tensions Mecke [31] suggested an expression based on the corresponding-states principle. In figure 3 the reduced surface tension is given versus reduced temperature. The results show that for elongations up to $L^* = 0.67$ there is a good representation of the simulation data which can be used for predictive purposes. A representative orientation profile of the two-centre Lennard-Jones molecules is given in figure 4(a)). The ordering parameter $P(z) = \frac{1}{2}\langle 3\cos^2\theta - 1\rangle$ shows that across the interface the molecules are oriented as follows: on the dense-liquid side they are preferably normal to the interface whereas on the gas side molecules tend to a parallel alignment. This is in agreement with results of a density functional theory for rod-like molecules given by Thurtell *et al* [104]. Similar results were found by Thompson and Gubbins [48, 105] on the basis of a perturbation theory approach and simulation data for site–site Lennard-Jones potential models of nitrogen and chlorine.
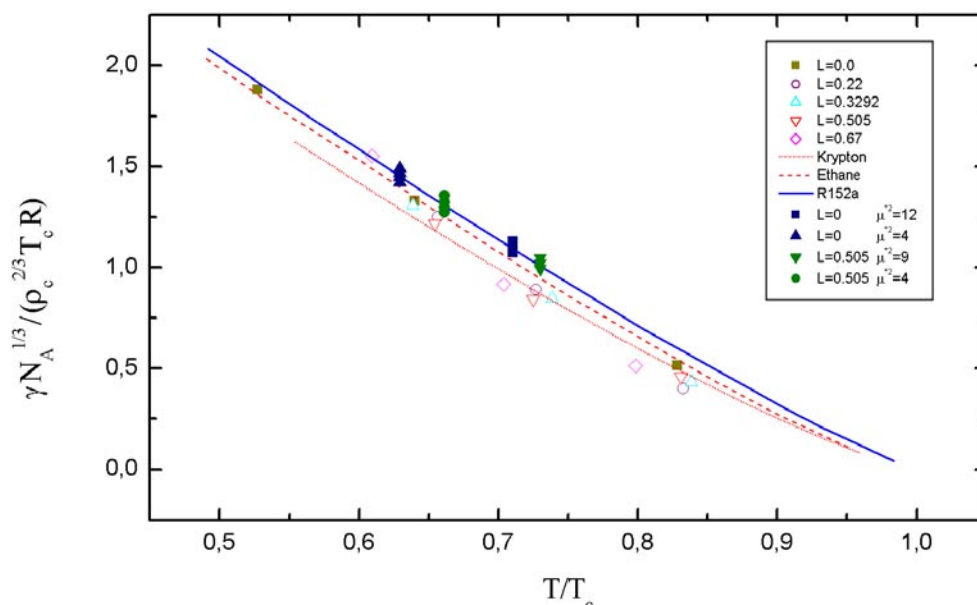

Figure 3. Surface tension of non-polar and dipolar fluids reduced to critical parameters versus reduced temperature T/T_c. Results for spherical and non-spherical molecular shapes are in very good agreement with experimental data for krypton (. . .), ethane (- - - -) and R152a (——).

Usually the long range of dipole–dipole interactions is larger than the length of a simulation cell. In homogeneous systems there are well-established techniques (reaction field or lattice summation) for tackling this problem. For an interfacial system only the choice of a laminar box like that in figure 1(c) allows one to apply conventional three-dimensional Ewald summation. The alternative (figure 1(b)) leads to a two-dimensional lattice summation with an absolute convergence. Unfortunately, the resulting expressions are much harder to implement into a simulation code. Mecke [31, 32] proposed an alternative technique, the pre-summation of dipolar contributions to energy and torque. He developed a very efficient procedure for simulations in these box geometries, periodic in only two dimensions. His simulations show
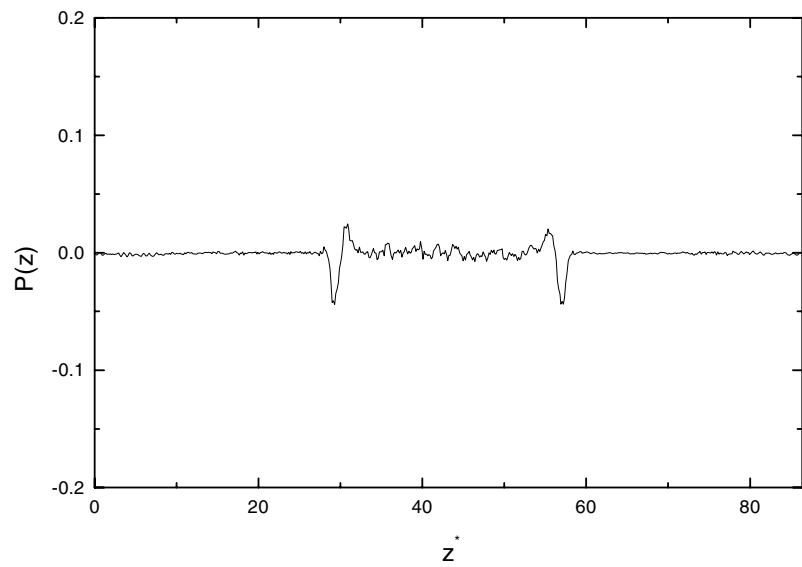
a)
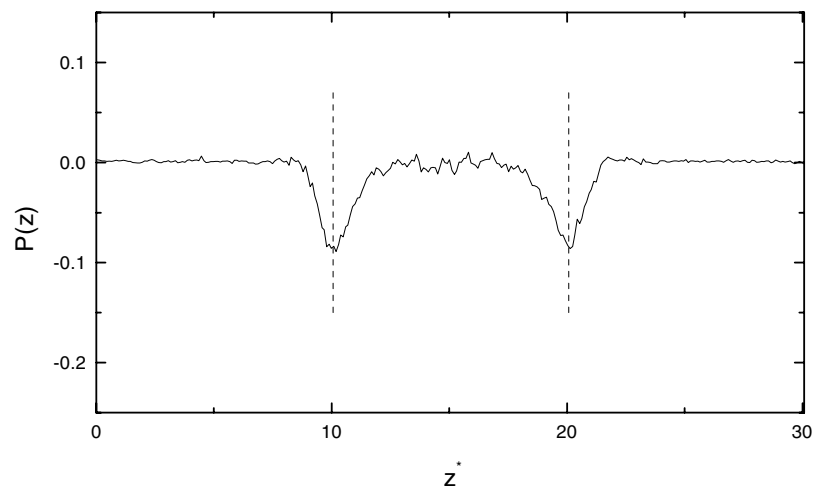
b)

Figure 4. Simulated orientational profiles $P(z)$ normal to the interface. (a) The orientational profile for a two-centre Lennard-Jones fluid with $L^* = 0.67\sigma$ at $T^* = 1.15$; (b) the orientational profile for a Stockmayer fluid with $\mu^{*2} = 12$ at $T^* = 1.05$.

that the two methods yield the same results without systematic deviations. When he analysed the simulated surface tensions of Stockmayer and of dipolar two-centre Lennard-Jones fluids he found that all data fit very well into his corresponding-states *ansatz*. Figure 3 shows all

simulation results together with experimental data for krypton, ethane and the refrigerant R152a. It demonstrates the excellent agreement between simulation and experiment.

When we analyse the orientational profiles of dipolar molecules, as shown in figure 4(b), we find a parallel orientation of dipoles across the interface, for both spherical and elongated molecular shapes. We have to admit that it differs from what was expected from integral equation [47] and density functional theory predictions [50], but it agrees with earlier simulation results of Thompson and Gubbins [48] and of Eggebrecht *et al* [49].

3. Density functional theory

We consider a system of N particles in a volume V without external fields and we assume that the interaction potential $u(r_1, r_2, \ldots, r_N)$ is given by a sum of intermolecular pair potentials:

$$u(r_1, r_2, \ldots, r_N) = \sum_{j \neq i}^{N} \sum_{i=1} u(r_i, r_j) \tag{4}$$

where three-body interactions are neglected. For such a system there exists a grand potential functional $\Omega[\tilde{\rho}(r)]$ of the particle-density distribution $\tilde{\rho}(r)$ which is the appropriate functional for an inhomogeneous fluid at constant temperature T and chemical potential μ [2–5]. This grand potential functional is related to the intrinsic Helmholtz free-energy functional $F[\tilde{\rho}(r)]$ by

$$\Omega\left[\tilde{\rho}\right] = F\left[\tilde{\rho}\right] - \mu \int dr \, \tilde{\rho}(r)$$

where $\tilde{\rho}(r)$ represents the local density of particles at r. The minimum value of $\Omega[\tilde{\rho}]$ is the equilibrium grand potential of the system and the corresponding equilibrium density distribution $\rho(r)$ is the solution of [2, 4, 5]

$$\left.\frac{\delta\Omega\left[\tilde{\rho}\right]}{\delta\tilde{\rho}(r)}\right|_{\rho} = \left.\frac{\delta F\left[\tilde{\rho}\right]}{\delta\tilde{\rho}(r)}\right|_{\rho} - \mu = 0. \tag{5}$$

From equation (3) the equilibrium density can be calculated once an expression for the intrinsic Helmholtz free energy is given. We separate this functional into the ideal-gas contribution $F_{id}[\rho]$ and a term $F_{ex}[\rho]$ which contains all contributions from intermolecular forces:

$$F\left[\rho\right] = F_{id}\left[\rho\right] + F_{ex}\left[\rho\right]. \tag{6}$$

The ideal-gas contribution to the free energy is given by

$$F_{id}\left[\rho\right] = kT \int dr \, \rho(r) \left[\ln(\Lambda^3 \rho(r)) - 1\right] \tag{7}$$

where k is the Boltzmann constant and Λ the de Broglie thermal wavelength of the particle. When we split the interaction potential (4) into a repulsive reference part $u^0(r_1, r_2)$ and an attractive term $u^a(r_1, r_2)$:

$$u(r_1, r_2; \lambda) = u^0(r_1, r_2) + \lambda u^a(r_1, r_2) \qquad 0 \leqslant \lambda \leqslant 1$$

the term $F_{ex}[\rho]$ can be expressed in a perturbation-like manner as [2, 4, 5, 8, 40, 54]

$$F_{ex}\left[\rho\right] = F_0\left[\rho\right] + F_a\left[\rho\right] \tag{8}$$

with

$$F_a\left[\rho\right] = \frac{1}{2} \int_0^1 d\lambda \int dr_1 \, \rho(r_1) \int dr_2 \, \rho(r_2) g(r_1, r_2; \lambda) u^a(r_1, r_2) \tag{9}$$

where λ is the familiar coupling parameter of the interaction potential. $g(r_1, r_2; \lambda)$ denotes the pair correlation function of a fluid with a pair potential $u(r_1, r_2; \lambda)$ and $F_0[\rho]$ is the intrinsic free-energy density of a reference fluid of density $\rho(r)$ and a pair potential $u(r_1, r_2; \lambda)$ with $\lambda = 0$.

For our model calculations we assume the interaction potential to be of Lennard-Jones (LJ) type. Like most other authors we choose a cut-off Lennard-Jones potential [6, 9], divided according to the prescription of Weeks, Chandler and Andersen into a reference part $u^0(r_{12})$ and an attractive contribution $u^a(r_{12})$

$$u^0(r_{12}) = \begin{cases} u^{LJ}(r_{12}) + \varepsilon & r_{12} \leqslant r_{12}^{\min} \\ 0 & r_{12} > r_{12}^{\min} \end{cases}$$

$$u^a(r_{12}) = \begin{cases} u^{LJ}(r_{12}) - u^0(r_{12}) & r_{12} \leqslant r_{12}^c \\ 0 & r_{12} > r_{12}^c. \end{cases} \tag{10}$$

At long range the potential is cut at a distance r_{12}^c. This WCA potential separation is the better alternative to another possible separation according to Barker and Henderson (BH), where the potential is divided at $r_{12} = \sigma$ into a repulsive part $u^0(r_{12})$ and the corresponding attractive contribution:

$$u^0(r_{12}) = \begin{cases} u^{LJ}(r_{12}) & r_{12} \leqslant \sigma \\ 0 & r_{12} > \sigma \end{cases}$$

$$u^a(r_{12}) = u^{LJ}(r_{12}) - u^0(r_{12}).$$

In both cases the repulsive potential $u^0(r_{12})$ is then approximated by that of an equivalent hard-sphere fluid with the diameter d chosen according to the Barker–Henderson prescription [60]

$$d = \sigma \int_0^{r_{12}^{\min}} dr_{12} \, (1 - \exp[-\beta u^0(r_{12})]). \tag{11}$$

For the hard-sphere system we use the Carnahan–Starling equation of state.

3.1. The repulsive part: LDA or weighted-density approximation

In the simple LDA, which is used in many applications, short-range correlations of molecules in the interface are completely neglected. This is known to be a rather poor approximation for fluids near walls or adsorption in porous systems [4–6, 33]. But for a free liquid interface in many cases the LDA seems to be a reasonable approach in modelling interfacial behaviour. Within the LDA [2, 4, 5, 8, 10] we have

$$F_0[\rho] = F_{HS}[\rho] \approx \int dr \, \rho(r) f_{HS}(\rho(r)) \tag{12}$$

where $f_{HS}(\rho)$ is the free energy per particle of a uniform hard-sphere fluid of density ρ.

Minimizing the grand potential functional with respect to $\rho(r)$ according to equation (5) yields for the repulsive part of the chemical potential

$$\mu^0 = \mu_{id}[\rho(r_1)] + \mu_{HS}[\rho(r_1)]. \tag{13}$$

In this case the short-ranged local structuring within the interface, which leads to an oscillatory density profile, is neglected.

Alternatively a smoothed or coarse-grained density $\bar{\rho}(r)$ which is a non-local functional of $\rho(r)$ can be introduced according to the smoothed-density approximation (SDA) given by

Tarazona [2, 4, 5, 7, 8, 34]

$$\bar{\rho}(\mathbf{r}_1) = \int d\mathbf{r}_2 \, \rho(\mathbf{r}_2) w(\mathbf{r}_1, \mathbf{r}_2; \bar{\rho}(\mathbf{r}_1)). \tag{14}$$

Here $w(\mathbf{r}_1, \mathbf{r}_2; \bar{\rho}(\mathbf{r}_1))$ is a density-dependent weight function which is specified by requiring the direct correlation function of the hard-sphere reference system to be close to the direct correlation function obtained from the PY approximation [7]. Thus for the repulsive part of the free-energy functional we obtain

$$F_0[\rho(\mathbf{r})] = F_{HS}[\rho(\mathbf{r})] = \int d\mathbf{r} \, \rho(\mathbf{r}) \, \Delta\Psi_{HS}(\bar{\rho}(\mathbf{r})). \tag{15}$$

$\Delta\Psi_{HS}(\bar{\rho}(\mathbf{r}))$ is the configurational part of the free energy per particle obtained from the Carnahan–Starling equation of state.

Minimizing the grand potential functional with respect to $\rho(\mathbf{r})$ according to equation (5) we have for the repulsive part [2]

$$\mu^0 = \mu_{id}[\rho(\mathbf{r}_1)] + \Delta\Psi_{HS}[\bar{\rho}(\mathbf{r}_1)] + \int d\mathbf{r}_2 \, \frac{\delta\bar{\rho}(\mathbf{r}_2)}{\delta\rho(\mathbf{r}_1)} \rho(\mathbf{r}_2) \, \Delta\Psi'_{HS}[\bar{\rho}(\mathbf{r}_2)]. \tag{16}$$

Either equation (13) within the LDA or equation (16) has to be combined with a term relating to the chemical potential representing the attractive contributions to $F_{ex}[\rho]$, equations (8), (9).

3.2. The attractive term: mean-field or perturbation approximation

Since little is known about the correlation functions in inhomogeneous systems, several approximations were introduced in equation (9). In the past almost all DFT calculations were carried out within the so-called mean-field (MF) approximation to the attractive part of the free energy. Here the local correlation structure around a particle in the fluid phase is completely neglected. This leads to a rather simple expression for the excess free energy which can easily be evaluated:

$$F_a[\rho] = \frac{1}{2} \int d\mathbf{r}_1 \, \rho(\mathbf{r}_1) \int d\mathbf{r}_2 \, \rho(\mathbf{r}_2) u^a(\mathbf{r}_1, \mathbf{r}_2). \tag{17}$$

However, this MF *ansatz* is well known for its rather poor representation of the bulk phase equilibrium [40, 53, 54]. We compared previous MF-DFT calculations [56–59] with our recently performed MD simulations of the vapour–liquid interface of a Lennard-Jones fluid and we found considerable differences both in the bulk phase behaviour and in the interfacial properties.

In order to overcome these shortcomings, Tang *et al* [2, 54] described the attractive contribution to the free energy as follows:

$$F_a[\rho] = \frac{1}{2} \int d\mathbf{r}_1 \, \rho(\mathbf{r}_1) \int d\mathbf{r}_2 \, \rho(\mathbf{r}_2) g_0(\mathbf{r}_1, \mathbf{r}_2, \rho) u^a(\mathbf{r}_1, \mathbf{r}_2) \tag{18}$$

where $g_0(\mathbf{r}_1, \mathbf{r}_2, \rho)$ denotes the pair correlation function of a system of repulsive particles. This correlation function refers to an inhomogeneous system where in the interfacial region the density changes very rapidly over molecular distances. Because little is known so far of its behaviour in realistic non-uniform systems, we follow a procedure, proposed by Sokolowski and Fischer [55], of approximating g_0 by its counterpart for a bulk fluid, evaluated at an appropriate mean density $\bar{\rho}(\mathbf{r})$:

$$g_0(\mathbf{r}_1, \mathbf{r}_2, \rho) = g_0(r_{12}, \bar{\rho}). \tag{19}$$

Then a coarse-grained density $\rho_v(\mathbf{r})$, which is the local density, averaged over a sphere r_v, is introduced as

$$\rho_v(\mathbf{r}) = \int \mathrm{d}\mathbf{r}'\, \rho(\mathbf{r}')w(|\mathbf{r} - \mathbf{r}'|). \tag{20}$$

Following the procedure [55], we evaluate this mean density $\bar{\rho}$ as the average over the coarse-grained densities around particles at $\mathbf{r}_1$ and at $\mathbf{r}_2$:

$$\bar{\rho} = \frac{1}{2}\left[\int \mathrm{d}\mathbf{r}_1'\, \rho(\mathbf{r}_1')w(|\mathbf{r}_1 - \mathbf{r}_1'|) + \int \mathrm{d}\mathbf{r}_2'\, \rho(\mathbf{r}_2')w(|\mathbf{r}_2 - \mathbf{r}_2'|) \right] \tag{21}$$

with the weight functions given in [40, 55].

This choice seems to be more sensitive to the local structure around particles at $\mathbf{r}_1$ and $\mathbf{r}_2$.

With the pair correlation function according to equation (19) we obtain for the free-energy functional in a first-order perturbation

$$F_a[\rho] = \frac{1}{2}\int \mathrm{d}\mathbf{r}_1\, \rho(\mathbf{r}_1)\int \mathrm{d}\mathbf{r}_2\, \rho(\mathbf{r}_2)g_{HS}(r_{12}, \bar{\rho})u^a(r_{12}).$$

Minimizing the grand potential functional with respect to $\rho(\mathbf{r})$ yields:

- Mean-field (MF) approximation [2, 4, 5, 59]:

$$\mu = \mu^0[\rho(\mathbf{r}_1)] + \int \mathrm{d}\mathbf{r}_2\, \rho(\mathbf{r}_2)u^a(r_{12}). \tag{22}$$

- Perturbation (PT) approximation [40, 55]:

$$\mu = \mu^0(\rho(\mathbf{r}_1)) + \int \mathrm{d}\mathbf{r}_2\, \rho(\mathbf{r}_2)g_{HS}(r_{12}, \bar{\rho})u^a(r_{12})$$
$$+ \frac{3}{8\pi r_v^3}\int_{|r_1 - r_2|\leqslant r_v} \mathrm{d}\mathbf{r}_2\, \rho(\mathbf{r}_2)\int \mathrm{d}\mathbf{r}_3\, \rho(\mathbf{r}_3)\frac{\partial g_{HS}(r_{23}, \bar{\rho})}{\partial \bar{\rho}}u^a(r_{23}). \tag{23}$$

Here

$$\mu^0 = \mu_{id} + \mu_{HS} \tag{24}$$

is the chemical potential of the repulsive reference fluid.

The advantage of using equation (23) for the chemical potential both in phase equilibrium and density profile calculation is that we stay consistently within the energy equation approach. However, it could be applied only after we found a suitable access to the density derivative of the hard-sphere pair correlation function [40].

3.3. Fluid mixtures

The description of fluid multicomponent mixtures within the DFT is a generalization of the theory for pure fluids, given above. Therefore we will outline some main points only. We consider a fluid n-component mixture with one-particle densities $\{\rho_i(r)\}$ ($i = 1, 2, \ldots, n$) without external fields at a given T and chemical potentials $\{\mu_i\}$. Summation over repeated indices is implicit throughout this part.

We split the fluid interaction potential in the same WCA fashion as in the pure-fluid case (equation (10)) into a reference part $u_{ij}^0(r_{ij})$ and an attractive contribution $u_{ij}^a(r_{ij})$ with $r_{ij} = |r_i - r_j'|$. It will be cut off and shifted at r_{ij}^c according to

$$u_{ij}^0(r_{ij}) = \begin{cases} u_{ij}^{LJ}(r_{ij}) + \varepsilon_{ij} & r_{ij} \leqslant r_{ij}^{min} \\ 0 & r_{ij} > r_{ij}^{min} \end{cases}$$
$$u_{ij}^a(r_{ij}) = \begin{cases} u_{ij}^{LJ}(r_{ij}) - u_{ij}^0(r_{ij}) - u_{ij}^{LJ}(r_{ij}^c) & r_{ij} \leqslant r_{ij}^c \\ 0 & r_{ij} > r_{ij}^c \end{cases} \tag{25}$$

with

$$r_{ij}^C = 7.5\sigma_{ij}.\tag{26}$$

The repulsive potential $u_{ij}^0(r)$ is then approximated by that of an equivalent hard-sphere fluid with the diameter d_{ij} chosen according to the Barker–Henderson prescription (equation (11)).

For the attractive term of the free-energy functional, in all cases the MF approximation is used:

$$F_{ex}[\{\rho_i(\boldsymbol{r})\}] = F_0[\{\rho_i(\boldsymbol{r})\}] + \frac{1}{2}\int\int \mathrm{d}\boldsymbol{r}_i\,\mathrm{d}\boldsymbol{r}'_j\,\rho_i(\boldsymbol{r}_i)\rho_j(\boldsymbol{r}'_j)u_{ij}^a(r_{ij})\tag{27}$$

whereas both LDA and SDA can be applied for the repulsive term.

In the simple local density approximation we have

$$F_0[\{\rho_i(\boldsymbol{r})\}] = \int \mathrm{d}\boldsymbol{r}\,f_0(\{\rho_i(\boldsymbol{r})\})\tag{28}$$

where $f_0(\{\rho_i(\boldsymbol{r})\})$ is the Helmholtz free-energy density of a reference fluid [4, 5, 8].

In the SDA we introduce a coarse-grained density $\bar{\rho}(\boldsymbol{r})$ to take into account the strong density variations around a particle in the interface region. An extension to mixtures of the SDA by Tarazona (see section 3.2 above) led to difficulties with the definition of smoothed local densities [15, 61, 62]. We therefore adopt the Rosenfeld–Kierlik–Rosinberg procedure. Rosenfeld [63–65] proposed a free-energy density functional for an inhomogeneous hard-sphere mixture which was simplified by Kierlik and Rosinberg [66–70], who used scalar weight functions instead of vectorial quantities. These weight functions are characteristic of each type of molecule. They are density independent which considerably reduces the computational effort. We have

$$F_0[\{\rho_i(\boldsymbol{r})\}] = \int \mathrm{d}\boldsymbol{r}\,\Phi(\{n_\alpha(\boldsymbol{r})\})\tag{29}$$

where Φ is the Helmholtz excess free-energy density of the uniform hard-sphere fluid with the weighted densities denoted by

$$n_\alpha(\boldsymbol{r}) = \int \mathrm{d}\boldsymbol{r}'\,\rho_i(\boldsymbol{r}')\omega_i^{(\alpha)}(|\boldsymbol{r}-\boldsymbol{r}'|)\qquad \alpha = 1, 2, 3, 4.\tag{30}$$

The weight functions $\omega_i^{(\alpha)}(r)$ are given in [69]. Φ results from the Percus–Yevick compressibility equation [71–73] or the equivalent scaled-particle theory [74, 75]:

$$\Phi = -n_0\ln(1-n_3) + \frac{n_1 n_2}{1-n_3} + \frac{n_2^3}{24\pi(1-n_3)^2}.\tag{31}$$

Considering a binary mixture and minimizing the grand potential functional with respect to the partial densities $\{\rho_i(\boldsymbol{r})\}$ yields

$$\begin{aligned}
\mu_1 &= \mu_1^{id}[\rho_1(\boldsymbol{r}_1)] + \mu_1^0[\rho_1(\boldsymbol{r}_1)] + \int \mathrm{d}\boldsymbol{r}'_1\,\rho_1(\boldsymbol{r}'_1)u_{11}^a(r_{11}) + \int \mathrm{d}\boldsymbol{r}'_2\,\rho_2(\boldsymbol{r}'_2)u_{12}^a(r_{12})\\
\mu_2 &= \mu_2^{id}[\rho_2(\boldsymbol{r}_2)] + \mu_2^0[\rho_2(\boldsymbol{r}_2)] + \int \mathrm{d}\boldsymbol{r}'_1\,\rho_1(\boldsymbol{r}'_1)u_{21}^a(r_{21}) + \int \mathrm{d}\boldsymbol{r}'_2\,\rho_2(\boldsymbol{r}'_2)u_{22}^a(r_{22})
\end{aligned}\tag{32}$$

with the total density given by $\rho(\boldsymbol{r}) = \rho_1(\boldsymbol{r}) + \rho_2(\boldsymbol{r})$.

3.4. Density profile and surface tension calculation

Except for the perturbation approximation we applied the cut-off and shifted LJ potential with $r_{ij}^C = 7.5\sigma_{ij}$. Lower values of r^C significantly influence both the density profile and the interfacial properties. In contrast to the procedure of potential parameter estimation in our

earlier papers [56–58] we estimate the pure-fluid Lennard-Jones parameters ε_{ij} and σ_{ij} by fitting them only to experimental saturated liquid densities ρ_{exp} (table 2). This guarantees a reasonable representation of both the phase equilibrium and the saturated liquid-density side of the phase envelope. At a given temperature the equilibrium (bulk) densities of the coexisting liquid and vapour phases are determined by simultaneously solving the equation of phase equilibrium.

Table 2. Molecular potential parameters ε/k and σ used in the MF and PT approximations of density functional theory, estimated by modelling saturated liquid densities [40, 59].

Substance	MF		PT-DFT	
	ε/k (K)	σ (Å)	ε/k (K)	σ (Å)
Ar	128.042	3.331	119.304	3.392
N_2	105.119	3.514	98.227	3.577
Kr	171.227	3.529	164.817	3.618
CO	104.060	3.494	105.561	3.610
Argon[a]	114.14	3.2582		
Methane	145.23	3.5771		
Heptane	451.226	5.7634		
Toluene	484.753	5.224		
DMF	498.89	4.764		

[a] Potential parameters used for the binary mixture.

For binary mixtures we have to solve simultaneously

$$p_L(T, \rho_L, x_1) = p_V(T, \rho_V, y_1)$$
$$\mu_{L,1}(T, \rho_L, x_1) = \mu_{V,1}(T, \rho_V, y_1) \tag{33}$$
$$\mu_{L,2}(T, \rho_L, x_1) = \mu_{V,2}(T, \rho_V, y_1).$$

Here ρ_L denotes the bulk liquid density and x_1 the corresponding mole fraction. ρ_V is the vapour density and y_1 the vapour-phase mole fraction.

The system is generally confined to a length of $z_{ij}^{\text{max}} = 5r_{ij}^C \sigma_{ij}$. Starting with a step function profile $\rho_i^k(z)$, equation (32) or—in the case of a pure fluid—equation (22) or (23) is solved iteratively:

$$\mu_i^0(\rho_i^{k+1}(z)) = \mu_i - \phi_i^{\text{eff}}(z) \tag{34}$$

with

$$\phi_i^{\text{eff}}(z) = \int \rho_1^k(z^*)u_{i1}^a(|z - z^*|)\, \mathrm{d}z^* + \int \rho_2^k(z^*)u_{i2}^a(|z - z^*|)\, \mathrm{d}z^*.$$

On inversion, $\mu_i^0(\rho_i^{k+1}(z))$ generates ρ_i^{k+1}, since $\mu^0(z)$ is a monotonically increasing function of ρ. The convergence of the solution is usually rapid and corresponds to the approach to a local minimum of the grand potential Ω. Having obtained the final density profile, we calculate the surface tension from [76, 77]

$$\gamma = \int_{-\infty}^{\infty} [\omega(z) + p]\, \mathrm{d}z \tag{35}$$

with

$$\omega(z) = \sum_{i=1}^{n} \left[-p_i^0(\rho_i(z)) + \rho_i(z)\left(\mu_i^0(\rho_i(z)) - \mu_i + \frac{1}{2}\phi_i^{\text{eff}}(z) \right) \right].$$

4. Prediction of interfacial structure and properties

4.1. Interfacial structure and surface tension

Since both the phase equilibrium and interfacial behaviour of a fluid system are governed by the same intermolecular interaction forces, one set of potential parameters should be sufficient for describing and predicting both groups of phenomena, provided that the theoretical model is physically realistic. Therefore we determine the potential parameters from phase behaviour and then we predict all interfacial properties. The potential parameters for all systems used in our model calculations are given in table 2.

First, we compare the phase equilibrium of a pure fluid with our equation-of-state (EOS) results [41], with MD simulations [78, 79] and with results from the MF approximation for both WCA- and BH-separated potentials. The results in figure 5 show that both MF phase envelopes considerably deviate from the simulation results but that the WCA separation works much better than the corresponding BH model. That is why the WCA model is almost exclusively used in DFT calculations. In the low-temperature range the PT approximation agrees very well with the MD and EOS data. At higher reduced temperatures it shows slight deviations, a behaviour also reported by Tang and Lu [80]. Compared with previous results [40], those obtained with the use of the Carnahan–Starling EOS for the hard-sphere reference system instead of the PY compressibility equation are slightly improved. To go further, a second-order perturbation term should be included in equation (18) as proposed by Davis [2], but this dramatically complicates all numerical procedures involved in solving equation (23) for the density profile.
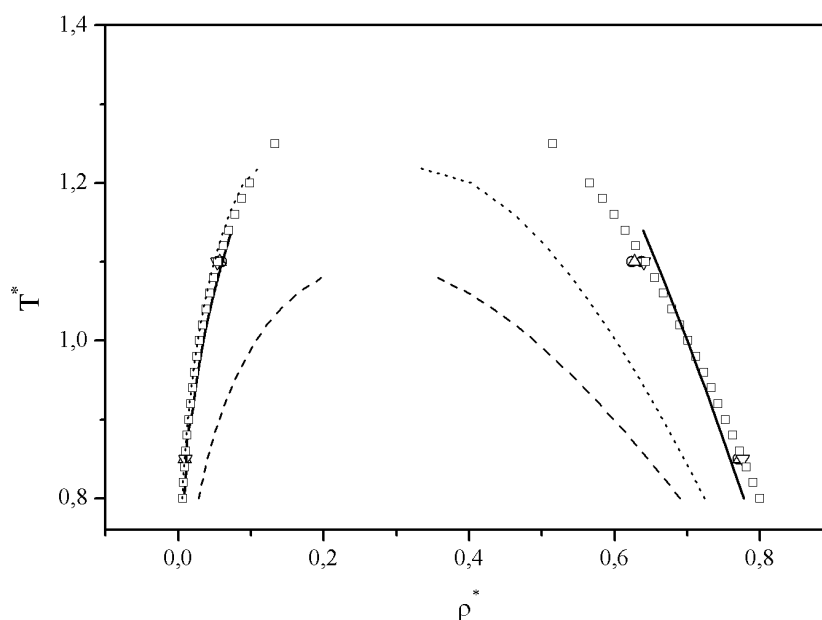

Figure 5. The phase diagram of the Lennard-Jones fluid. Comparison of the present approach (solid line) with BH-MF (dashed line) and WCA-MF (dotted line) calculations, with a MD-simulation-based EOS [41] (open squares), with direct simulation results of Lotfi *et al* [78] (upward-pointing triangle), with NpT + test-particle simulations of Lotfi *et al* [79] (downward-pointing triangles) and with MD simulations of the liquid–vapour interface [31, 38] (open circles).

Once the density profiles are obtained by solving either equation (22) or (23) for pure fluids or the corresponding equation (32) for mixtures, we calculate the intrinsic surface tension from equation (35). The graphs in figure 6 show the DFT results in comparison with our MD simulation data [38]. The γ^* from PT-DFT calculations are in very good agreement with the simulations. The MF results, however, exhibit rather large deviations at low temperatures which decrease with increasing T^*. This indicates that at high temperatures the influence of local structuring around a particle in the interface decreases. In the vicinity of the critical point a zero-density approximation to the correlation function, as applied by Frodl and Dietrich [50], seems to be an appropriate model.
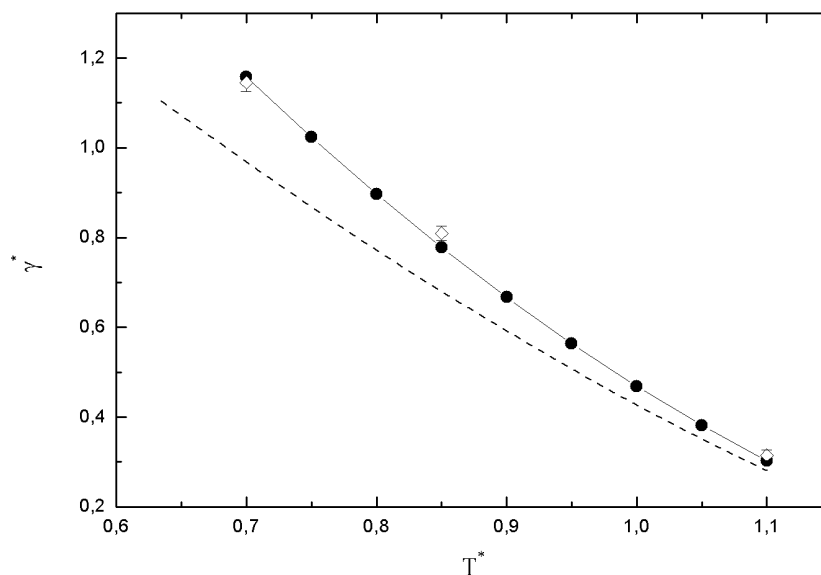

Figure 6. Predicted surface tension γ^* of the Lennard-Jones fluid versus reduced temperature T^*. Results from DFT-PT calculations (solid circles) in comparison with mean-field results (dashed line) and MD simulation data [38] (diamonds).

The partial density profiles for the binary mixture argon + methane at 88.85 K are shown in figure 7, where a comparison between LDA and SDA results is given. The SDA profiles exhibit an oscillatory behaviour on the liquid side of the interface. The profile of argon shows an enrichment, especially at low concentrations, with a slight structuring. Surprisingly, in the same concentration range the methane profile exhibits a well-developed structure which extends into the liquid phase. It disappears completely at low methane concentrations. Here, despite a slight ripple in the argon profile, it looks rather similar to that of the LDA model. When we compare the calculated surface tension of a mixture there is almost no difference between the graphs resulting from either the LDA or the SDA model. However, it is rather sensitive to the binary potential parameters. For the binary mixture argon + methane a good representation of the x–y equilibrium curve was achieved with $k_{ij} = 0.018$ and $l_{ij} = 0.0$. The results for γ slightly deviate from the experimental data [81]. But a small change of $l_{ij} = 0.009$ yields an excellent representation of the surface tension and gives only a small deviation in the vapour–liquid equilibrium. All binary parameters are given in table 3.

For the ternary mixture N, N-dimethyl formamide (DMF) + heptane + toluene at $T = 298.15$ K we calculated the partial density profiles within the LDA model. Figure 8 (top) shows the concentration profiles at a constant $x_{DMF} = 0.8$. We clearly see the considerable enrichment
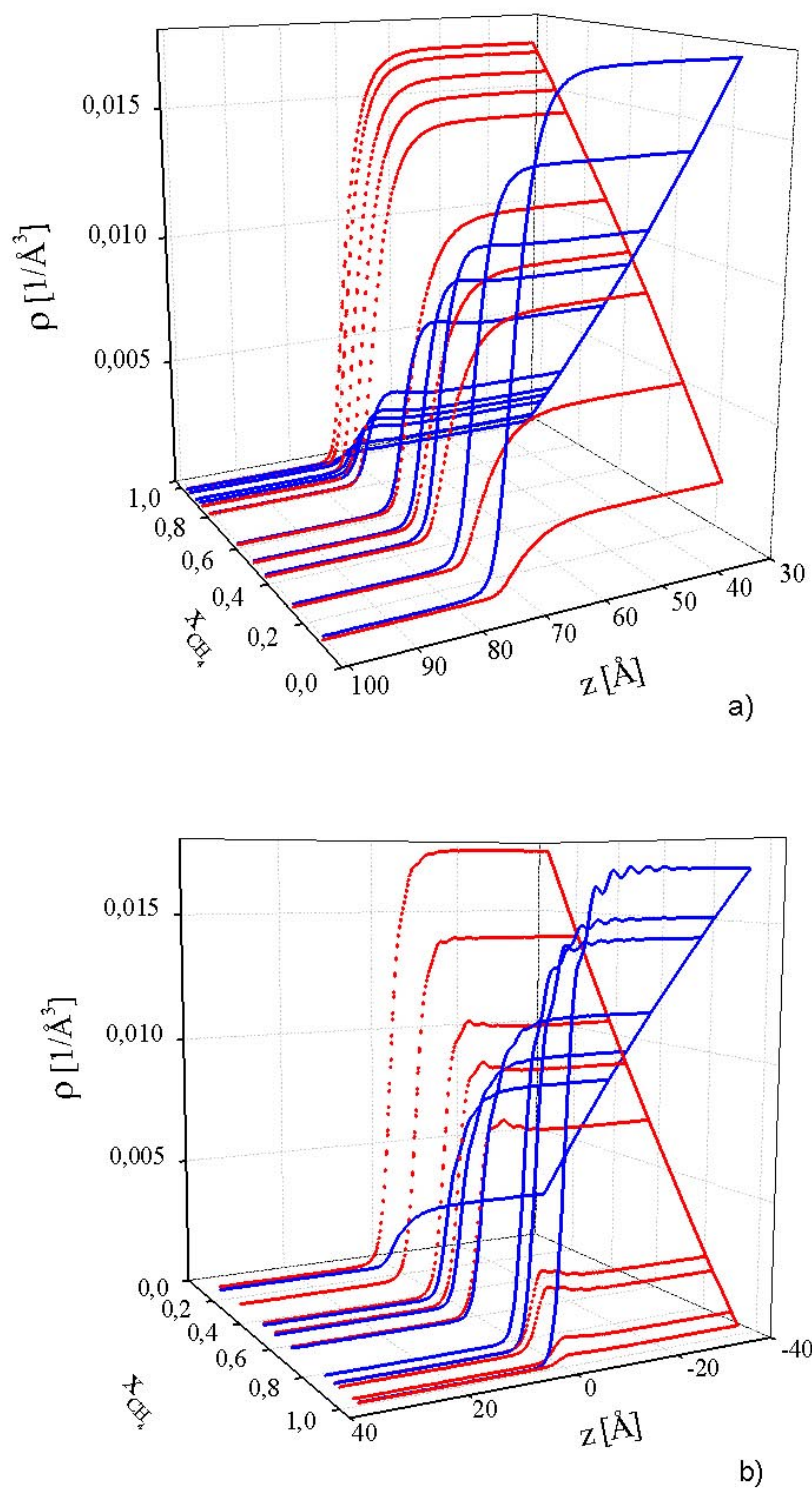
Figure 7. Partial density profiles in the argon–methane system at $T = 88.85$ K versus mole fraction of methane. (a) LDA profiles; (b) SDA profiles.

Table 3. Empirical binary parameters k_{ij} and l_{ij} of the binary mixtures investigated.

Binary mixture	k_{ij}	l_{ij}
Ar–N$_2$	0.062	−0.02
CH$_4$–Ar	0.018	0.0
		0.009
n-heptane–toluene	0.017	0.0005

of heptane in the interface, especially at low concentrations. The DMF molecules are partly driven out of the interface and heptane and toluene molecules compete for the interfacial positions. In a two-dimensional cut (figure 8 (bottom)) we find that heptane is preferentially placed above the toluene molecules in this interfacial area, thus building a 'chemical' barrier to other molecules, penetrating the interface.

4.2. Interfacial thickness and capillary-wave contributions

For pure fluids there are two different measures for the thickness of a liquid–vapour interface. The '10%-to-90%' width [9] is rather arbitrary whereas a more rigorous expression of Chapela *et al* [82] uses the steepness of a density profile at mid-density:

$$\tau = -(\rho_l - \rho_v)\left[\frac{\partial\rho(z)}{\partial z}\right]_{z=z_0}^{-1} \tag{36}$$

with

$$\rho(z_0) = \frac{1}{2}(\rho_l - \rho_v).$$

When we apply either of the two measures to the well-structured profiles we find that most of the structuring and even most of the enrichment of one component would be attributed to the liquid bulk outside the interface. From both partial densities and the overall density profile in figure 7 one can easily imagine that a thickness τ, calculated from equation (36), would leave large parts of the structuring out of consideration.

We therefore propose a new measure for the interfacial thickness in liquid mixtures, which will include almost all of the structuring in the interface. From the partial density profiles we can obtain a symmetrized surface segregation $\Delta C(z)$, which measures the local relative concentration of the two species in the interface and thus reflects a deviation in concentration from the bulk phases [83]:

$$\Delta C(z) = \frac{\rho_1(z) - \rho_{l,1}}{\alpha_1} - \frac{\rho_2(z) - \rho_{l,2}}{\alpha_2} \tag{37}$$

with symmetrized concentrations α_i:

$$\alpha_i = \frac{\rho_{l,i} - \rho_{v,i}}{(\rho_{l,1} + \rho_{l,2}) - (\rho_{v,1} + \rho_{v,2})}$$

where $\rho_{l,i}$, $\rho_{v,i}$ denote the liquid and vapour bulk densities, respectively. This surface segregation $\Delta C(z)$ is shown in figure 9(a) for the argon–methane system at 88.85 K over the whole concentration range. We find that the deviation from an average bulk concentration, where $\Delta C(z)$ is zero, and thus the interfacial thickness is found to be about 2.4 nm. This thickness is almost constant over the concentration range. When we compare the surface segregations of the LDA and SDA models, as shown in figure 9(b), we find that the structuring of the density profiles is less dominant in $\Delta C(z)$ and that the two models give nearly the same width. It
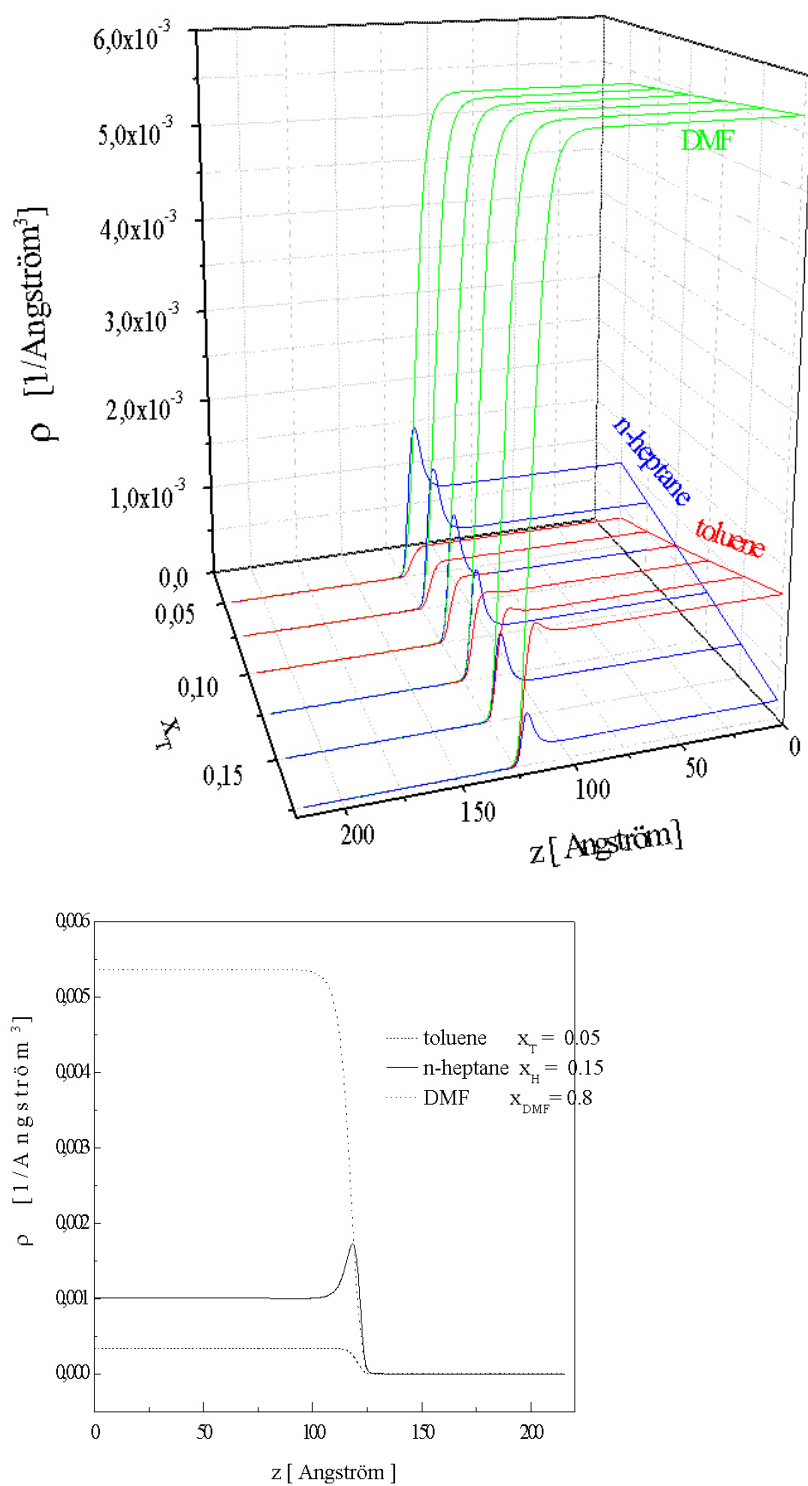
Figure 8. Partial density profiles for the ternary system N, N-dimethyl formamide (DMF) + toluene + n-heptane at 298 K. The bottom graph represents a two-dimensional cut at the given composition with the enrichment of heptane in the interface.

seems that $\Delta C(z)$ is a more appropriate measure for the interfacial thickness than the density profile itself. We therefore propose a new definition of the interfacial thickness τ:

$$\tau = \text{range}\{|\Delta C(z)| > 0.05\,\Delta C(z)_{\text{max}}\} \tag{38}$$

as the range in z where the amount of $\Delta C(z)$ deviates by more than 5% from its maximum value. This definition, of course, is still arbitrary, but since ΔC may show quite different behaviour and even changes sign over the concentration range, there is no rigorous expression for the interfacial thickness in a mixture and thus we believe that our definition is the most appropriate.

As a consequence of a spontaneous symmetry breaking of a two-phase system, long-ranged correlations parallel to the interface occur. This horizontal correlation corresponds to surface modes, thermally excited against surface tension and gravity with an effective capillary-wave Hamiltonian:

$$H(h(r_{xy})) = \frac{1}{2} \int \mathrm{d}r_{xy} \, [\gamma_i |\nabla_{xy} h(r_{xy})|^2 + mg\,\Delta\rho\,h(r_{xy})^2]$$

for small fluctuations $\nabla h(r_{xy}) \ll 1$ and no curvature contributions. The vertical excitation $h(r_{xy})$ due to capillary waves leads to a thickening of the interface. This surface roughening leads to an increase in the effective interfacial thickness and thus affects the surface tension. Taking these capillary-wave fluctuations into account, the macroscopically measured surface tension γ_{exp} can be approximated by a contribution from the intrinsic density profile γ_i and a capillary-wave-fluctuation term. There are several theoretical approaches for tackling this problem which finally lead to very similar results. Whereas Evans [84] starts with a free-energy functional, Dietrich [85] uses an effective interface Hamiltonian which describes the free energy of increasing the surface area against the surface tension due to curvature and gravitational contributions. Both arrive at expressions for the height–height correlation function that are proportional to the square of the interfacial thickness. Meunier [86] proposed a mode-coupling theory for the mean squared roughness:

$$\langle h^2 \rangle_{cw} = \frac{kT}{2\pi} \int_{Q_{\text{min}}}^{Q_{\text{max}}} \mathrm{d}Q \, \frac{Q}{\gamma(Q)\,|Q|^2 + mg\,\Delta\rho} \tag{39}$$

where $\gamma(Q)$ depends on the wave vector Q. Finally

$$\gamma(Q) = \gamma_{\text{exp}} + \frac{3kT}{8\pi} Q^2.$$

In the gravitational limit $Q = 0$, we have $\gamma(Q = 0) = \gamma_{\text{exp}}$. We have to introduce an upper limit Q_{max} to Q that separates the short-wavelength region, described by the intrinsic profile, from the capillary-wave contribution. This limit Q_{max} can be associated with the intrinsic surface tension $\gamma(Q_{\text{max}}) = \gamma_i$. Thus we obtain

$$\gamma(Q) = \gamma_i + \frac{3kT}{8\pi}(Q^2 - Q_{\text{max}}^2). \tag{40}$$

This is a relation which can be used to approximately predict the macroscopic surface tension from an intrinsic surface tension γ_i and a suitable model value of the cut-off Q_{max} of the capillary-wave contribution.

The evaluation of Q_{max} is somewhat ambiguous; it can either be related to the inverse of the bulk correlation length ξ or to some other structural parameter like the inverse of the width of the intrinsic profile, because capillary waves should not have smaller λ than the thickness of the rigid interface. To predict the surface tension from our DFT calculation we proceed as follows. For a given temperature the theoretical calculations provide us with an intrinsic
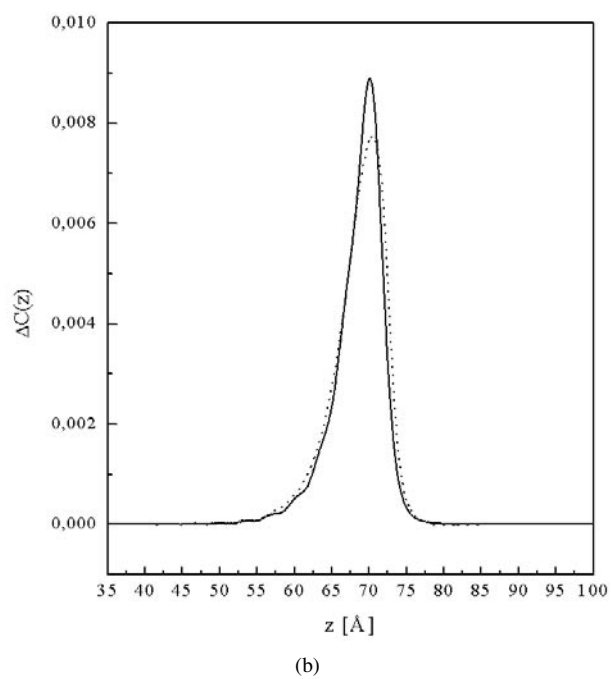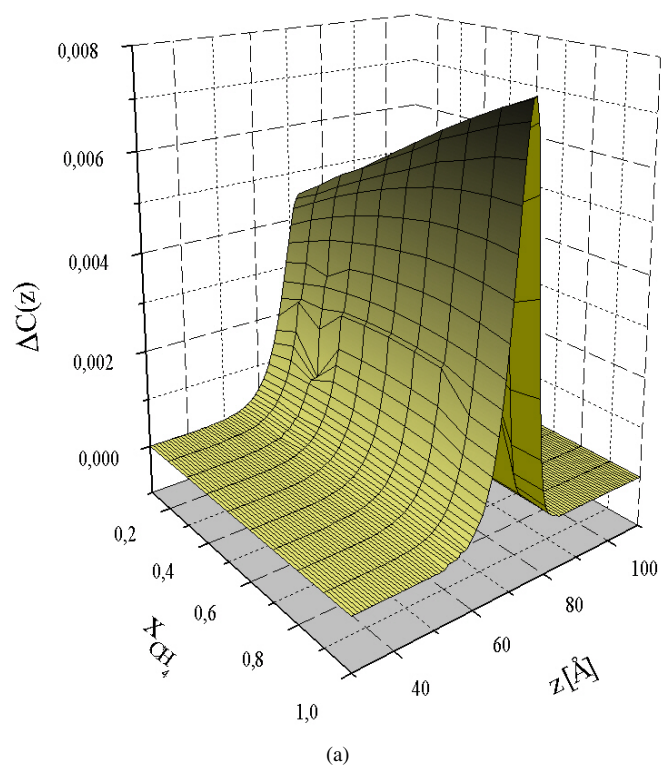
(a)

(b)

Figure 9. (a) Surface segregation $\Delta C(z)$ in the argon–methane system at 88.85 K, calculated within the SDA approximation. (b) Comparison of the surface segregation $\Delta C(z)$ calculated from the SDA (solid line) and the LDA (dotted line) at a constant-composition cut through the results shown in (a).

surface tension γ_i and an interfacial width τ. Then we approximate the cut-off wave vector Q_{max} by [59, 84]

$$Q_{max} = \frac{\pi}{\tau^* \sigma} \tag{41}$$

where τ^* is the reduced interfacial thickness. This choice of Q_{max} divides the whole range into a molecular region where the intrinsic structure is considered in detail and the capillary-wave region on a length scale larger than the interfacial thickness. With this Q_{max} we obtain the capillary-wave contribution to the surface tension and from equation (40) the macroscopic $\gamma(Q = 0)$ is predicted, which can be compared with the experimental γ_{exp}.

When we compare the γ^* for pure fluids with experimental data we find that both our MD and PT-DFT results agree very well with each other but they are systematically higher than the experimental data. This seems to be clear evidence for missing capillary-wave contributions to the surface tension. From the density profile we calculate the interfacial thickness τ via (36) and then we use it as a measure for the short-wavelength cut-off Q_{max} in equation (41). This enables us to predict a macroscopic surface tension from equation (40). It should be noted that all calculations are based on Lennard-Jones potential parameters which were adjusted to describe the phase equilibria and no additional external information is used for the prediction of interfacial properties. A comparison of the results is given in figure 10. For the WCA-MF model we find the well-known result [106] that the predicted surface tension deviates considerably from experimental data. Results from the PT-DFT model are closer to the experimental results but their temperature dependence still deviates from what we expect. Only when we add capillary-wave contributions to the PT-DFT calculations do the resulting data agree as regards their temperature dependence rather well with experiment. A perfect agreement between experiment and calculation cannot be achieved or expected because real fluids differ in their intermolecular interactions from the model potentials that we use in our theory.
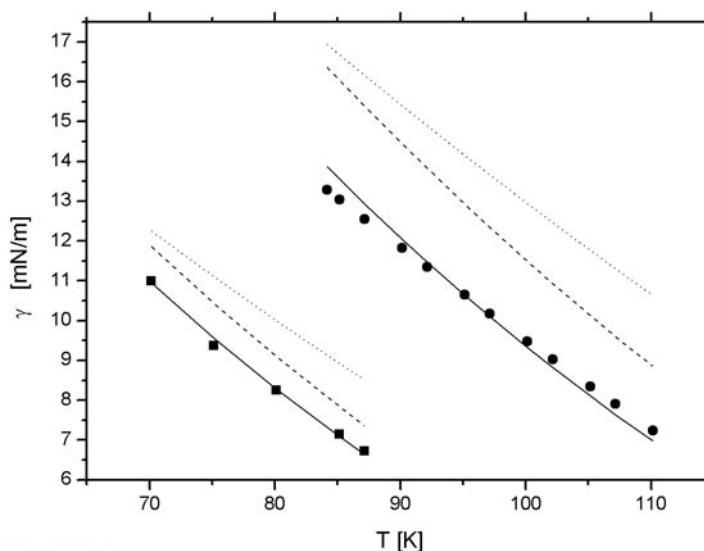

Figure 10. The predicted surface tension γ in comparison with experimental data. WCA-MF results (dotted line); PT results without capillary-wave contributions (dashed line) and with capillary terms added (solid line). Experimental data for argon [81, 102] (solid circles) and for nitrogen [81, 102, 103] (solid squares).

4.3. Prediction of ellipsometric parameters

Ellipsometry is an optical technique widely used for the study of interfaces between two dielectric media [87–89]. It determines the complex ratio of amplitude reflectivities for p- and s-polarized electromagnetic waves. This ratio depends on the profile of the optical dielectric constant in the interface. Knowing this, it should be possible to predict the reflection behaviour and the ellipticity of the interface as a function of wavelength λ and of the angle of incidence φ_0 of a polarized laser light beam.

The electric field vector E is split into components E_p parallel and E_s perpendicular to the plane of incidence of the light beam with $\tilde{E}_p$, $\tilde{E}_s$ the real amplitudes of the p and s components and δ_p, δ_s their relative phases; the parameter Δ denotes the phase shift between the p and s components: $\Delta = \delta_p - \delta_s$. The other parameter, Ψ, characterizing the polarization of the light beam is defined by the ratio of the real amplitudes of the two components: $\tan \Psi = \tilde{E}_p / \tilde{E}_s$.

Then the ellipticity is obtained as the ratio of the minor and major axes of the ellipse of polarization $e = \tan \vartheta = a/b$ with $\sin 2\vartheta = \sin 2\Psi \sin \Delta$. Ellipsometry measures the ratio of the complex-amplitude reflection coefficients of the p and s components [57, 90–92]:

$$\rho = \frac{r_p}{r_s} = \frac{\tan \Psi^r}{\tan \Psi^i} \exp[i(\Delta^r - \Delta^i)]$$

with the superscripts i, r denoting the components of the incident and reflected beam.

From the reflection behaviour at ideal and real interfaces we know that at low angles of incidence φ_0 the phase shift $\Delta = 180°$. At the so-called Brewster angle φ_B, the phase shift becomes $\Delta = 90°$ and reduces further to $\Delta = 0°$ with increasing φ_0. At φ_B, the parameter ϑ coincides with Ψ; that is, the major axis of the ellipse of polarization becomes parallel to E_s. Then $\rho = i \tan \vartheta$ and $e = \bar{\rho}$.

From DFT we obtain the partial density profiles of each of the components in a mixture. These profiles are transformed into one refractive index profile. To calculate the reflection behaviour of this profile we divide it into a large number of very thin layers of constant refractive index. Then we use the multilayer formalism of Crook [90, 93]. It provides us with the reflectance of our system. The procedure continues up to the surface layer.

As result of the DFT calculations in the LDA or SDA approximations, we have at our disposal partial density profiles on an equally spaced grid. These profiles are transformed into a profile of the optical dielectric constant $n(z)$ using either the Lorentz–Lorenz equation which corresponds to an ideal system without inductive interactions:

$$\frac{n^2(z) - 1}{n^2(z) + 2} = \frac{4}{3} \pi \sum_i \rho_i(z) \alpha_i \tag{42}$$

or the Onsager reaction-field model where inductive interactions are included:

$$\frac{(n^2(z) - 1)(2n^2(z) + 1)}{12\pi n^2(z)} = \sum_i \frac{\rho_i(z) \alpha_i}{1 - f_i \alpha_i}. \tag{43}$$

Here the α_i are the corresponding molecular polarizabilities and the reaction-field factors are given by

$$f_i = \frac{2n^2(z) - 2}{\sigma_i^3 (2n^2(z) + 1)}.$$

This refractive index profile $n(z)$ is used as input into Crook's recursive algorithm to predict the ellipsometric parameters. For any given angle of incidence we obtain $\Psi(\varphi_0)$, $\Delta(\varphi_0)$ and $e(\varphi_0)$. Thus we construct diagrams of these ellipsometric parameters as functions of φ_0. Applying the condition $\Delta = 90°$ we find at $\varphi_0 = \varphi_B$ the ellipticity $\bar{e}_B$ at the Brewster angle.

The only additional input parameters needed are the molecular polarizabilities of the mixture components [94]. Solving equation (42) or (43) for $n(z)$ we obtain the respective profiles of the refractive index. We assume a He–Ne laser with a wavelength of 632.8 nm.

The aim of the investigation is twofold:

(i) we want to know whether different models of the optical dielectric constant affect the final results and

(ii) we want to know how the structuring of the partial density profiles changes the ellipsometric parameters and whether ellipsometry might give us at least an indirect proof of this structuring.

Our results clearly show that there is no difference in the profiles $n(z)$ irrespective of whether we use the ideal Lorentz–Lorenz equation (42) or Onsager's model (43). Obviously the influence of the reaction field is negligible on the optical dielectric constant, at least for the non-polar simple fluids considered here. Because of the structuring in the SDA profile we choose 2000 layers for Crook's algorithm. The final values of the ellipticity e for the binary argon–methane mixture are shown in figure 11 (top). The ellipticity increases with the angle of incidence φ_0, passes through a maximum near the Brewster angle and decreases again with rising φ_0. In both the LDA and SDA models the ellipticity passes through a maximum at low argon concentrations. The slopes of the two sets of graphs are rather similar and there is no visible effect of the structuring of $n(z)$ in the resulting ellipticity e versus φ_0. Figure 11 (bottom) gives the ellipticity at the Brewster angle as a function of the methane concentration. Except for two data points for pure argon [95], there are no experimental values to compare with our predictions. The intrinsic part of the SDA ellipticity is somewhat lower than the corresponding LDA data. But if we take into account contributions due to capillary waves, which lead to a broadening of the interface, then the SDA result considerably improves, as shown in figure 11 (bottom).

On the basis of a coupled-mode theory of thermal fluctuations, Meunier [86] gave expressions for capillary-wave contributions to different optical properties. For the ellipticity at the Brewster angle $\overline{e}$ he obtained

$$\overline{e}^{cw} = \frac{3\pi}{2\lambda} \frac{n_L^2 - n_V^2}{\sqrt{n_L^2 + n_V^2}} \sum_q q \langle \zeta_q^2 \rangle \tag{44}$$

with

$$\sum_q q \langle \zeta_q^2 \rangle = \frac{1}{4} \sqrt{\frac{8kT}{3\gamma\pi}}. \tag{45}$$

n_L and n_V are the refractive indices of the liquid and vapour phases, respectively. $q \langle \zeta_q^2 \rangle$ is the average of the square amplitude of a mode q excited by thermal motion. For reference, these ellipticities are included in figure 11 (bottom). If we want to add capillary-wave contributions to the ellipticity in our LDA and SDA models, we can refer to our q_{max} in (41) which yields [96–98]

$$\sum_q q \langle \zeta_q^2 \rangle = \frac{1}{2\pi} \sqrt{\frac{8kT}{3\gamma\pi}} \arctan\left(q_{max} \sqrt{\frac{3\pi kT}{8\gamma}}\right). \tag{46}$$

This contribution shifts the SDA values of $\overline{e}$ very close to Meunier's results (see figure 11 (bottom)), which shows the internal consistency of our approach.
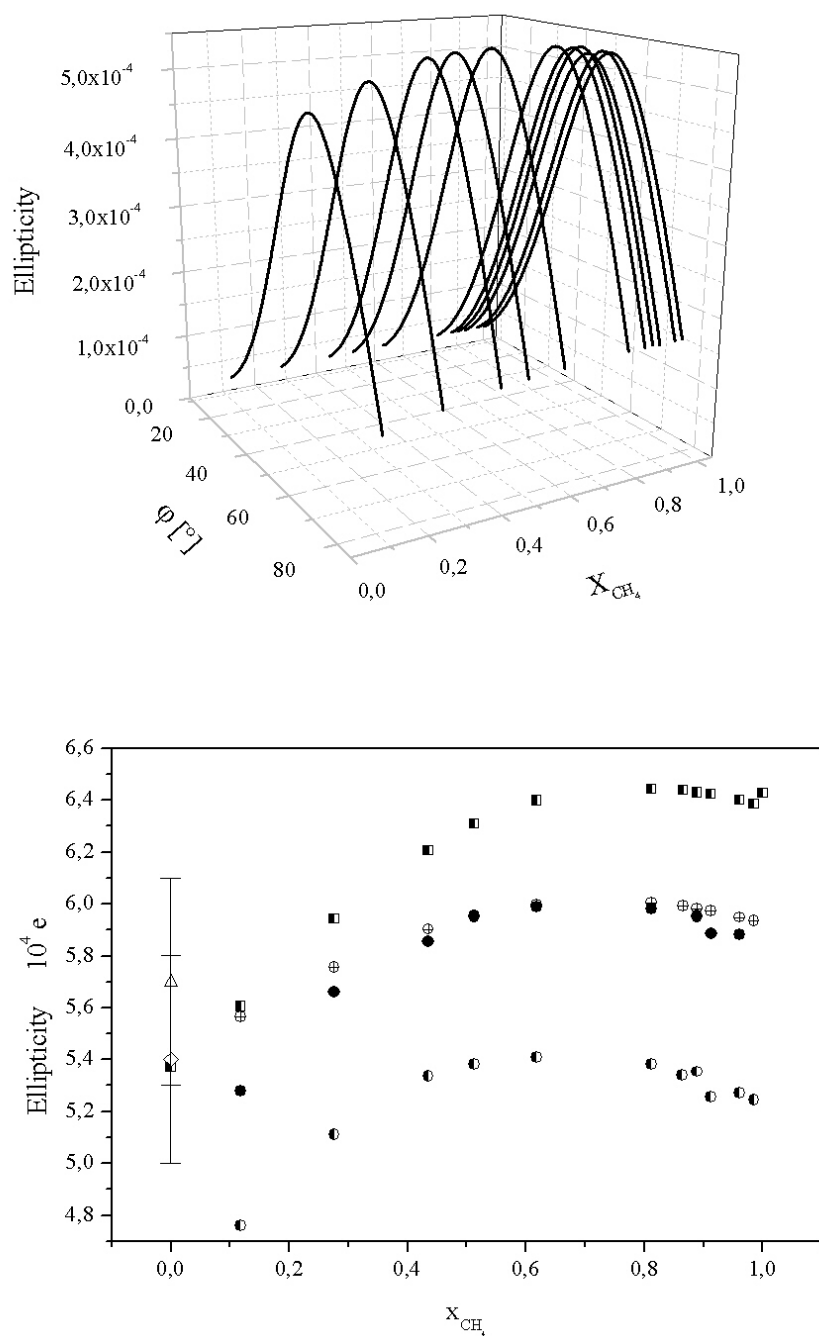
Figure 11. Top: the ellipticity in the methane–argon system at $T = 88.85$ K calculated from SDA refractive index profiles versus angle of incidence and mole fraction. Bottom: the ellipticity at the Brewster angle in the binary argon–methane mixture at $T = 88.85$ K calculated from LDA (squares) and SDA (solid points) refractive index profiles and from mode-coupling theory (points with centre crosses, according to Meunier [86]). Also shown are experimental values for pure argon (open triangle and open diamond) from [95].

4.4. Prediction of specular x-ray reflectivities

X-ray reflectivity is among the few optical techniques available for investigating the structure of liquid surfaces. It was recently applied with considerable success, because it is sensitive not only to the intrinsic density profile and its structuring, but also to height fluctuations resulting from thermally induced capillary waves [35, 36]. Both the theory of x-ray reflectivity and its experimental methods have been described in detail [36, 37, 99, 100], so we can restrict ourselves to a discussion of the so-called 'master formula' [101] and its application.

In specular reflection the incident radiation is directed downwards to the $x–y$ plane at an angle of θ and the reflected wave is observed under an angle $\theta' = \theta$ in the same z-plane as the incident beam. Thus the specular conditions require that the wave vector is given by

$$|Q| = Q_z = \frac{4\pi}{\lambda} \sin \theta$$

with $Q_x = Q_y = 0$. The reflectivity of an ideal, perfectly flat step surface without absorption can be obtained from Fresnel's reflection law for x-rays incident from vacuum under an angle θ on a sharp surface. The reflectivity from a real surface departs from Fresnel's law when the surface is not ideally flat or there exists a density profile for the transition from liquid to vapour. Therefore we can expect two different contributions to the reflectivity $R(Q_z)$ resulting from (i) the internal structure or density profile and (ii) surface roughening caused by thermally induced capillary waves. If we normalize the reflectivity $R(Q_z)$ with that of the idealized sharp surface $R_F(Q_z)$, we obtain the well-known master formula introduced by Als-Nielsen and Kjaer [101]:

$$\frac{R(Q_z)}{R_F(Q_z)} = \left| \frac{1}{\rho^e(\infty)} \int_{-\infty}^{\infty} \mathrm{d}z \, \frac{\mathrm{d}\rho^e(z)}{\mathrm{d}z} \mathrm{e}^{-\mathrm{i}Q_z z} \right|^2 \tag{47}$$

where $\rho^e(\infty)$ is the average electron density in the bulk of the material far from the surface. $\rho^e(z)$ is the electron-density profile and $\mathrm{d}\rho^e(z)/\mathrm{d}z$ is the derivative along the normal to the surface of the average electron density. The local electron-density profile $\rho^e(z)$ can be calculated from [36] $\rho^e(z) = \rho(z) \sum e^-$.

We apply equation (47) to determine specular reflectivities from our theoretically calculated density profiles [59]. This comparison of predicted reflectivities with experimental data opens up an additional opportunity to verify the calculated profiles. This is even more important because here not only the overall shape of the profile but also the internal structuring and possible oscillations will affect the reflectivity.

In addition to the internal density profile, a surface roughening caused by thermally excited capillary waves leads to an increase in surface diffuse scattering and thus contributes to the observed specular reflectivity. Braslau *et al* [36] show in their capillary-wave model that the two-dimensional energy density for surface waves is composed of a surface tension term and a gravitational contribution according to equation (39) [59]. They took the resolution of their two-slit apparatus into account and obtained an approximate expression:

$$\langle h^2 \rangle_{cw} = \frac{kT}{2\pi \gamma_i} \ln \left[\frac{Q_{\max}}{Q_z(\Delta\theta_d)} \right]$$

where $\Delta\theta_d = h_d/L$ is the full width of the angular resolution in the plane of incidence of their x-ray beam. The final form for the reflectivity is thus

$$\frac{R(Q_z)}{R_F(Q_z)} = \left| \frac{1}{\rho^e(\infty)} \int_{-\infty}^{\infty} \mathrm{d}z \, \frac{\mathrm{d}\rho^e(z)}{\mathrm{d}z} \mathrm{e}^{-\mathrm{i}Q_z z} \right|^2 \mathrm{e}^{-\langle h(Q_z)^2 \rangle Q_z^2}. \tag{48}$$

This is the product of the contribution from the intrinsic profile of the electron density and the surface capillary-wave term. With our expression for the short-wavelength limit $Q_{\max}$, we are
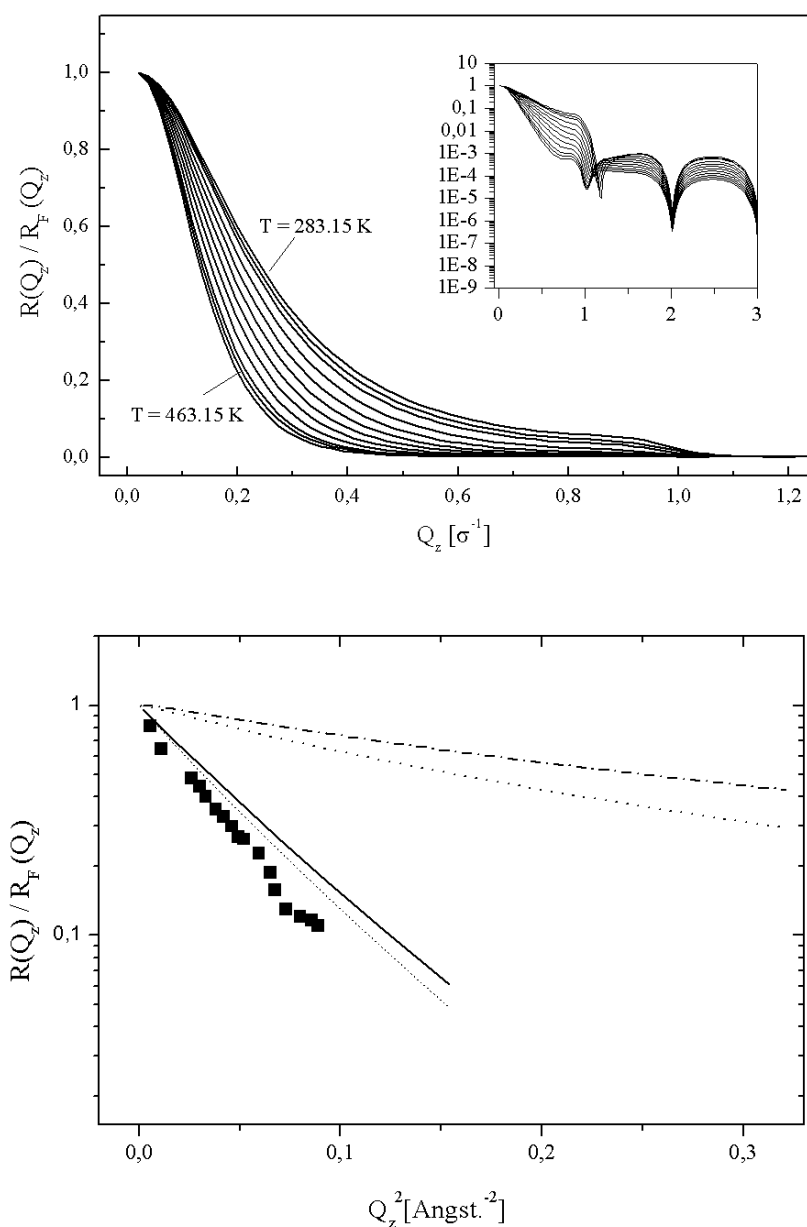
Figure 12. Top: specular reflectivities for CCl_4 (normalized to the Fresnel reflectivity) calculated from SDA density profiles without capillary-wave contributions at $\lambda = 1.53$ Å from $T = 283.15$ K up to 463.15 K. Bottom: specular reflectivities for CCl_4 versus Q^2. The squares are experimental data from [36]. The dashed–dotted line (SDA) and the dotted line (LDA) are the reflectivities calculated from the DFT density profiles. The solid line (SDA) and the dashed line (LDA) represent the reflectivities calculated from the DFT density profiles and our model capillary-wave contributions.

able to evaluate the second term and thus predict specular reflectivities exclusively from model parameters of the intrinsic surface structure.

The specular reflectivities calculated from SDA profiles with their oscillatory structuring are shown in figure 12 (top) for CCl_4. The general shape at small Q looks similar to those of the LDA model. But, there is a typical structuring at higher Q (see the inset in figure 12 (top)) which obviously results from short-range oscillations of the density profile at the interface. It also reflects the size of the molecular spheres. This structuring of specular reflectivities would provide valuable information on the interfacial structuring of the intrinsic density profiles. But unfortunately this range of high Q and low reflectivities is outside the range of experimental measurements. When we compare both SDA and LDA calculations with the few available experimental data, we obtain computed reflectivities (figure 12 (bottom)) which are much too high. The reflectivity of a real interface is not purely specular because diffuse scattering due to capillary-wave fluctuations also contributes to the measured intensity. Using the capillary-wave model of Braslau *et al* [36] according to equation (48) with our cut-off Q_{max}, equation (41), we find that the addition of capillary-wave contributions considerably improves the calculated reflectivities, as shown in figure 12 (bottom). Unfortunately there are no other experimental data for simple fluids to compare with and to use for testing the reliability of the proposed procedure.

5. Conclusions

The application of the density functional theory to interfaces of pure simple fluids provides a useful tool for the calculation of surface properties and structural behaviour of a vapour–liquid interface. Due to a better description of the attractive part of the free-energy functional we get a better representation of the bulk properties. This opens up the possibility to compare interfacial calculations to computer simulation results. The surface tensions calculated this way agree well with recent molecular dynamics simulations. The prediction of specular reflectivities and ellipsometric parameters can help in the interpretation of experimental data using a statistical mechanical model of the liquid interface. On the other hand, the comparison of theoretical calculations with experimental data will lead to a better understanding of capillary-wave fluctuations which have to be taken into account both in DFT calculations and in MD simulations of surface properties. Starting from this basis, with the introduction of more realistic potentials and a deeper study of capillary-wave contributions, we will obtain a more comprehensive picture of both bulk and interface properties.

Acknowledgments

References

[1] Boda D, Henderson D, Rowley R and Sokolowski S 1999 *J. Chem. Phys.* **111** 9382
[2] Davis H T 1996 *Statistical Mechanics of Phases and Interfaces, and Thin Films* (Weinheim: VCH)
[3] Evans R 1979 *Adv. Phys.* **28** 143
[4] Evans R 1992 *Fundamentals of Inhomogeneous Fluids* ed D Henderson (New York: Dekker)
[5] Evans R 1990 *Liquids at Interfaces* ed J Charvolin, J F Joanny and J Zinn-Justin (Amsterdam: North-Holland)
[6] Peterson B K, Gubbins K E, Heffelfinger G S, Marini Bettolo Marconi U and van Swol F 1988 *J. Chem. Phys.* **88** 6487
[7] Tarazona P and Evans R 1984 *Mol. Phys.* **52** 847
[8] Tarazona P, Marini Bettolo Marconi U and Evans R 1987 *Mol. Phys.* **60** 573

[9]   Lu B Q, Evans R and Telo da Gama M M 1985 *Mol. Phys.* **55** 1319
[10] Sullivan D E 1979 *Phys. Rev.* B **20** 3991
      Sullivan D E 1981 *J. Chem. Phys.* **74** 2604
[11] Fischer J and Methfessel M 1980 *Phys. Rev.* A **22** 2836
[12] Fischer J and Heinbuch U 1987 *J. Chem. Phys.* **88** 1909
[13] Wendland M, Salzmann S, Heinbuch U and Fischer J 1989 *Mol. Phys.* **67** 161
[14] Wendland M, Heinbuch U and Fischer J 1989 *Fluid Phase Equilibria* **48** 259
[15] Sokolowski S and Fischer J 1990 *Mol. Phys.* **70** 1097
[16] Wendland M 1997 *Fluid Phase Equilibria* **141** 25
[17] Wendland M 1998 *Fluid Phase Equilibria* **147** 105
[18] Iatsevitch S and Forstmann F 2000 *Mol. Phys.* **98** 1309
[19] Lee D J, Telo da Gama M M and Gubbins K E 1984 *Mol. Phys.* **53** 1113
[20] Lee D J, Telo da Gama M M and Gubbins K E 1985 *J. Phys. Chem.* **89** 1514
[21] Chapela G A, Saville G, Thompson S M and Rowlinson J S 1977 *J. Chem. Soc. Faraday Trans.* II **73** 1133
[22] Salomons E and Mareschal M 1991 *J. Phys.: Condens. Matter* **3** 3645
[23] Salomons E and Mareschal M 1991 *J. Phys.: Condens. Matter* **3** 9215
[24] Holcomb C D, Clancy P, Thompson S M and Zollweg J A 1992 *Fluid Phase Equilibria* **75** 185
      Holcomb C D, Clancy P, Thompson S M and Zollweg J A 1993 *Fluid Phase Equilibria* **88** 303
      Holcomb C D, Clancy P and Zollweg J A 1993 *Mol. Phys.* **78** 437
[25] Trokhymchuk A and Alejandre J 1999 *J. Chem. Phys.* **111** 8510
[26] Panagiotopoulos A Z 1987 *Mol. Phys.* **61** 813
[27] Möller D and Fischer J 1990 *Mol. Phys.* **69** 463
      Möller D and Fischer J 1992 *Mol. Phys.* **75** 1461
[28] Matsumoto M and Kataoka Y 1988 *J. Chem. Phys.* **88** 3233
[29] Alejandre J, Tildesley D J and Chapela G A 1995 *J. Chem. Phys.* **102** 4574
[30] Tarek M, Tobias D J and Klein M L 1995 *J. Phys. Chem.* **99** 1393
[31] Mecke M 2000 Computersimulationen zur Struktur und zu Grenzflächeneigenschaften in den Phasengrenzen
      molekularer und polarer Fluide sowie binärer Mischungen *VDI Reihe Progress Report* Series 3, No 646
      (Düsseldorf: VDI)
[32] Mecke M, Fischer J and Winkelmann J 2001 *J. Chem. Phys.* **114** 5842
[33] Peterson B K and Gubbins K E 1987 *Mol. Phys.* **62** 215
[34] Tarazona P 1985 *Phys. Rev.* A **31** 2672
[35] Pershan P S 1991 *Physica* A **172** 17
[36] Braslau A, Pershan P S, Swislow G, Ocko B M and Als-Nielsen J 1988 *Phys. Rev.* A **38** 2457
[37] Pershan P S 1993 *Physica* A **200** 50
[38] Mecke M, Winkelmann J and Fischer J 1997 *J. Chem. Phys.* **107** 9264
[39] Mecke M, Winkelmann J and Fischer J 1999 *J. Chem. Phys.* **110** 1188
[40] Wadewitz T and Winkelmann J 2000 *J. Chem. Phys.* **113** 2447
[41] Mecke M, Müller A, Winkelmann J, Vrabec J, Fischer J, Span R and Wagner W 1996 *Int. J. Thermophys.* **17**
      391
[42] Fincham D, Quirke N and Tildesley D J 1986 *J. Chem. Phys.* **84** 4535
[43] Lotfi A, Vrabec J and Fischer J 1990 *Mol. Simul.* **5** 233
[44] Kirkwood J G and Buff F P 1949 *J. Chem. Phys.* **17** 338
[45] Blokhuis E M, Bedeaux D, Holcomb C D and Zollweg J A 1995 *Mol. Phys.* **85** 665
[46] Kriebel C, Müller A, Winkelmann J and Fischer J 1995 *Mol. Phys.* **84** 381
[47] Iatsevitch S and Forstmann F 2000 *Transport Mechanisms Across Fluid Interfaces (DECHEMA Monographs
      vol 136)* (New York: Wiley–VCH)
[48] Thompson S M and Gubbins K E 1981 *J. Chem. Phys.* **74** 6467
[49] Eggebrecht J, Thompson S M and Gubbins K E 1987 *J. Chem. Phys.* **86** 2299
[50] Frodl P and Dietrich S 1992 *Phys. Rev.* A **45** 7330
      Frodl P and Dietrich S 1993 *Phys. Rev.* E **48** 3203
      Frodl P and Dietrich S 1993 *Phys. Rev.* E **48** 3741
[51] Curtin W A and Ashcroft N W 1986 *Phys. Rev. Lett.* **56** 2775
[52] Velasco E and Tarazona P 1989 *J. Chem. Phys.* **91** 7916
[53] Kierlik E, Fan Y, Monson P A and Rosinberg M L 1995 *J. Chem. Phys.* **102** 3712
[54] Tang Z, Scriven L E and Davis H T 1991 *J. Chem. Phys.* **95** 2659
[55] Sokolowski S and Fischer J 1992 *J. Chem. Phys.* **96** 5441
[56] Winkelmann J, Brodrecht B and Kreft I 1994 *Ber. Bunsenges. Phys. Chem.* **98** 912

[57] Winkelmann J 1994 *Ber. Bunsenges. Phys. Chem.* **98** 1308
[58] Wadewitz T and Winkelmann J 1996 *Ber. Bunsenges. Phys. Chem.* **100** 1825
[59] Wadewitz T and Winkelmann J 1999 *Phys. Chem. Chem. Phys.* **1** 3335
[60] Verlet L and Weiss J 1972 *Phys. Rev.* A **5** 939
[61] Heffelfinger G S, Tan Z, Gubbins K E, Marini Bettolo Marconi U and van Swol F 1988 *Int. J. Thermophys.* **9** 1051
[62] Tan Z, Marini Bettolo Marconi U, van Swol F and Gubbins K E 1989 *J. Chem. Phys.* **90** 3704
[63] Rosenfeld Y 1989 *Phys. Rev. Lett.* **63** 980
[64] Rosenfeld Y 1996 *J. Phys.: Condens. Matter* **8** 9289
[65] Rosenfeld Y, Schmidt M, Löwen H and Tarazona P 1996 *J. Phys.: Condens. Matter* **8** L577
[66] Kierlik E and Rosinberg M L 1991 *Phys. Rev.* A **44** 5025
[67] Kierlik E and Rosinberg M L 1998 private communication
[68] Phan S, Kierlik E, Rosinberg M L, Bildstein B and Kahl G 1993 *Phys. Rev.* E **48** 618
[69] Kierlik E and Rosinberg M L 1990 *Phys. Rev* A **42** 3382
[70] Kierlik E, Rosinberg M L, Finn J E and Monson P A 1992 *Mol. Phys.* **75** 1435
[71] Wertheim M S 1963 *Phys. Rev. Lett.* **10** 321
[72] Thiele E 1963 *J. Chem. Phys.* **39** 474
[73] Lebowitz J L 1964 *Phys. Rev.* **133** 895
[74] Reiss H, Frisch H and Lebowitz J L 1959 *J. Chem. Phys.* **31** 369
[75] Helfand E, Frisch H L and Lebowitz J L 1961 *J. Chem. Phys.* **34** 1037
[76] Evans R, Marini Bettolo Marconi U and Tarazona P 1986 *J. Chem. Soc. Faraday Trans.* II **82** 1763
[77] Telo da Gama M M and Evans R 1979 *Mol. Phys.* **38** 367
[78] Lotfi A, Vrabec J and Fischer J 1990 *Mol. Simul.* **5** 233
[79] Lotfi A, Vrabec J and Fischer J 1992 *Mol. Phys.* **76** 1319
[80] Tang Y and Lu C-Y 1997 *AIChE J.* **43** 2215
     Tang Y and Lu C-Y 1997 *Mol. Phys.* **90** 215
[81] Sprow F B and Prausnitz J M 1966 *Trans. Faraday Soc.* **62** 1097
[82] Chapela G A, Saville G, Thompson S M and Rowlinson J S 1977 *J. Chem. Soc. Faraday Trans.* II **8** 1133
[83] Telo da Gama M M and Evans R 1983 *Mol. Phys.* **48** 229
[84] Evans R 1981 *Mol. Phys.* **42** 1169
[85] Dietrich S 1996 *J. Phys.: Condens. Matter* **8** 9127
[86] Meunier J 1987 *J. Physique* **48** 1819
     Meunier J 1990 *Liquids at Interfaces* ed J Charvolin, J F Joanny and J Zinn-Justin (Amsterdam: North-Holland)
[87] Beaglehole D 1983 *J. Phys. Chem.* **87** 4749
[88] Law B M and Beaglehole D 1981 *J. Phys. D: Appl. Phys.* **14** 115
[89] Beaglehole D 1981 *J. Chem. Phys.* **75** 1544
[90] Heidel B and Findenegg G H 1987 *J. Chem. Phys.* **87** 706
[91] Heidel B 1986 *Dissertation* Bochum University
[92] Süßmann R 1989 *Dissertation* Bochum University
[93] Crook A W 1948 *J. Opt. Soc. Am.* **38** 954
[94] *CRC Handbook of Thermophysical and Thermodynamic Data* 1994 ed D R Lide and H V Kehiaian (Boca Raton, FL: Chemical Rubber Company Press)
[95] Beaglehole D 1980 *Physica* B **100** 163
[96] Bonn D and Wegdam G H 1992 *J. Physique* I **2** 1755
[97] Beaglehole D 1987 *Phys. Rev. Lett.* **58** 1434
[98] Beysens D and Meunier J 1988 *Phys. Rev. Lett.* **61** 2002
[99] Pedersen J S and Hamley I W 1994 *J. Appl. Crystallogr.* **27** 36
[100] Pedersen J S and Hamley I W 1994 *Physica* B **198** 16
[101] Als-Nielsen J and Kjaer K 1989 *Phase Transitions in Soft Condensed Matter* (New York: Plenum) pp 113–38
[102] Stairs R A and Sienko M J 1956 *J. Am. Chem. Soc.* **78** 920
[103] Baidakov V B 1982 *Zh. Fiz. Khim.* **56** 814
[104] Thurtell J H, Telo da Gama M M and Gubbins K E 1985 *Mol. Phys.* **54** 321
[105] Thompson S M and Gubbins K E 1981 *J. Chem. Phys.* **75** 1325
[106] Aracil J, Luengo G, Almeida B S, Telo da Gama M M, Rubio R G and Diaz Pena M 1989 *J. Phys. Chem.* **93** 3210